Earth Planet. Sci. Lett. 640 (2024) 118767

Contents lists available at ScienceDirect

Earth and Planetary Science Letters

journal homepage: www.elsevier.com/locate/epsl

Importance of grain boundary processes for plasticity in the quartz-dominated crust: Implications for flow laws

Subhajit Ghosh [a,b,*], Holger Stünitz [a,c], Hugues Raimbourg [a], Jacques Précigout [a], Ida Di Carlo [a], Renée Heilbronner [d], Laurette Piani [e]

[a] Institut des Sciences de la Terre d'Orléans (ISTO), UMR7327, Université d'Orléans, CNRS, BRGM, 45071, Orléans, France
[b] Department of Geology and Geophysics, Woods Hole Oceanographic Institution, Woods Hole, MA, USA
[c] Department of Geology, University of Tromsø, Dramsveien 201, 9037, Tromsø, Norway
[d] Department of Environmental Sciences, Universität Basel, CH-4056 Basel, Switzerland
[e] Centre de Recherches Pétrographiques et Géochimiques (CRPG), UMR 7358, Université de Lorraine, CNRS, Vandoeuvre-les-Nancy, France

ARTICLE INFO

Keywords:
Quartz rheology
Flow law
Grain boundary migration
Grain boundary sliding
Hydrolytic weakening
Core-shell-structure

ABSTRACT

When H_2O is present along grain boundaries, the deformation processes responsible for plasticity in silicate mineral aggregates can deviate from what may be conventionally expected. Although a necessary component of understanding crustal deformation processes, there is no theoretical framework that incorporates grain boundary processes into polycrystalline quartz rheology. To address this issue, we carried out high-pressure and high-temperature deformation experiments on fine-grained quartz aggregates. Our study illustrates that grain boundary migration (GBM) through dissolution-precipitation (in the presence of an aqueous fluid) and grain boundary sliding (GBS) may act as accommodation mechanisms to prevent hardening from dislocation glide. GBM and GBS can relax incompatibilities resulting from an inadequate number of independent slip systems, plastic anisotropy between neighbouring grains, and non-planar grain boundaries together with grain boundary junctions. As demonstrated earlier in the literature, GBM may act as a recrystallization mechanism counteracting hardening, but also is a potential mechanism that allow H_2O to enter in the quartz crystal (hydrolization) at the experimental time-scale. The above serial processes occur over a range of more than two orders of magnitude in grain size (~3 to 200 μm) and explain a grain-size-insensitive stress exponent ($n = 2$) and low activation energy ($Q = 110$ kJ/mol). In the absence of a switch to grain size sensitive deformation mechanisms induced by grain size reduction, our results imply that only a modest weakening (~5 times the strength of the protolith) is needed (or possible) to localize shear zones in the Earth's crust.

1. Introduction

How parts of the crust become weaker compared to the surrounding rocks and develop into plate boundaries is one of the fundamental questions when trying to explain plate tectonics on Earth. In nature, weakening of silicate minerals involves two essential components: (a) the presence of H_2O, and (b) reduced grain size (e.g., Griggs 1974; Bercovici and Ricard, 2016; Finch et al., 2016; Hirth and Tullis, 1992; Holyoke and Kronenberg, 2013; Kronenberg et al., 2020). Quartz is one of the best studied rock-forming minerals of the Earth's crust, and understanding quartz rheology and microstructures are instrumental to characterize the mechanical properties of crustal rocks (Hirth et al., 2001). Consequently, an overwhelming number of experimental studies have focused on establishing creep laws for coarse- and fine-grained natural and synthetic quartz aggregates in different hydrous conditions over the last four decades (e.g., Jaoul et al., 1984; Kronenberg and Tullis, 1984; Luan and Paterson, 1992; Gleason and Tullis, 1995; Rutter and Brodie, 2004a, 2004b; Fukuda et al., 2018; Richter et al., 2018). Recently, using the new generation hydraulically-driven Griggs-type apparatus, it has become possible to perform constant-load experiments with larger sample size at a regulated constant confining pressure (Précigout et al., 2018). New experiments have yielded flow-law parameters for wet (0.1 wt.% H_2O-added) coarse-grained (~200 μm) quartzite from the Tana quarry, Norway based on the following equation:

* Corresponding author.
E-mail addresses: cugeol.subhajit@gmail.com, subhajit.ghosh@whoi.edu (S. Ghosh).

https://doi.org/10.1016/j.epsl.2024.118767
Received 30 November 2023; Received in revised form 22 March 2024; Accepted 11 May 2024
Available online 1 June 2024

$$\dot{\varepsilon} = A\left(\frac{\sigma^n}{d^p}\right) f_{H_2O}^r \exp\left(-\frac{Q}{RT}\right), \quad (1)$$

where $\dot{\varepsilon}$ is the strain rate, σ is the differential stress, f_{H_2O} is the water fugacity term with an exponent $r = 1$, d is the grain size, n is the stress exponent, p is the grain size exponent, Q is the activation energy, and A is the pre-exponential term. The new flow law is as follows (Ghosh et al., 2022):

$$\dot{\varepsilon} = 1.56 \times 10^{-6}\ _{/MPa/sec} \cdot \sigma^2 \cdot f_{H_2O} \cdot \exp\left(-\frac{110\ kJ/mol}{RT}\right). \quad (2)$$

Although a n-value lower than 3 has been obtained for other coarse-grained quartz materials (Jaoul et al., 1984; Koch et al., 1989; Luan and Paterson, 1992), it deviates from the accepted climb-controlled dislocation creep models with $n \approx 3$–5 (Hirth et al., 2001; Karato, 2008; Luan and Paterson, 1992; Paterson and Luan, 1990; Rutter and Brodie, 2004b). The n-values lower than 3 have been found for fine-grained quartz (Kronenberg and Tullis, 1984; Fukuda et al., 2018; Richter et al., 2018) and the contribution from diffusion creep ($n = 1$) (Herring, 1950; Nabbarro, 1948; Coble, 1963) was interpreted to produce lower n-values (Fukuda et al., 2018; Richter et al., 2018). However, grain-size-exponent of $p = 2$ or 3 as in grain size sensitive deformation mechanisms has not been identified (Jaoul et al., 1984; Kronenberg and Tullis, 1984; Fukuda et al., 2018; Ghosh et al., 2022). On the other hand, the low grain size exponent of $p \approx 0.5$ (Fukuda et al. 2018) is difficult to interpret. It has been concluded that grain boundary processes including dissolution-precipitation and grain boundary sliding (GBS) can lower the n-value (Ghosh et al., 2022; Nègre et al., 2021; Pongrac et al., 2022; Richter et al., 2018; Tokle et al., 2019).

Earlier studies have shown that extremely dry quartz single crystals or polycrystalline quartz aggregates are too strong to deform plastically under laboratory conditions (Blacic and Christie, 1984; Griggs, 1974; Kronenberg and Tullis, 1984) and a certain amount of H_2O is required ('hydrolytic weakening') to induce plasticity (Griggs and Blacic, 1965). Water weakening of quartz is generally associated with molecular forms of H_2O and/or with dissociated forms of H_2O (Stünitz et al., 2017, 2024). It has been proposed that hydrolization of Si-O bounds is responsible for the water weakening by easing the dislocation glide process (Griggs and Blacic 1965; Griggs, 1967, 1974). Additionally, the weakening effect can be originated from dislocation generation and multiplication associated with microcracking, crack healing, and fluid inclusion decrepitation (Stünitz et al., 2017). These explanations are suitable in the case of a single crystal quartz. However, in a polycrystalline material, according to the von Mises criterion at least five independent sets of slip systems are needed to achieve homogeneous deformation dominantly by glide mechanism (Karato, 2008). Much fewer slip systems are actually activated in quartz (Pongrac et al., 2022; Tokle et al., 2019). Furthermore, grains oriented in a favourable position for easy slip with respect to the local stress state will deform easily in comparison to the poorly oriented neighbouring grains (Qi et al., 2017). As a result, plastic incompatibilities between neighbouring grains can arise. To overcome these incompatibilities, additional processes (Hutchinson, 1976) such as grain boundary sliding (GBS) are needed, as shown in other geological materials like halite, ice, anorthite, and olivine (Bourcier et al., 2013, Dimanov et al., 2007, Goldsby and Kohlstedt, 2001; Hansen et al., 2011). GBS has also been speculated to operate in quartz (Ghosh et al., 2022; Tokle et al., 2019), even though non-planar grain boundaries together with grain boundary junctions impede GBS in normal circumstances (Ashby, 1972; Raj and Ashby, 1971). Therefore, for GBS to be an effective accommodation mechanism for crystal-plastic deformation by dislocation glide, there is a need for the activation of processes that counteract obstacles at grain boundaries.

The spectrum of quartz grain sizes found in natural rocks varies from coarse (millimeters) to very fine (a few micrometers). Therefore, the effect of the grain size on the mechanical properties (e.g., viscosity) of quartz aggregates is also an important factor to consider. For example, it is presumed that grain size reduction (GSR) in mylonitic shear zones can lead to significant weakening through the transition from grain-size-insensitive (GSI) to grain-size-sensitive (GSS) creep mechanisms (Schmid 1982; Rutter and Brodie, 1988) with n-value of 1. However, such a switch in dominant deformation mechanism has strictly been observed at a grain size of ~1 μm in dry quartz experiments (Rutter and Brodie 2004b; Fukuda et al., 2018) giving rise to the possibility that the deformation mechanism in fine-grained quartz bearing rocks (> 1 μm) may not be comparable to other geological materials like olivine, anorthite, ice, and diopside at a similar grain size range (Dimanov et al., 2007; Goldsby and Kohlstedt, 2001; Hier-Majumder et al., 2005; Hirth and Kohlstedt, 2004).

When H_2O is present along grain boundaries, additional boundary processes (e.g. dissolution-precipitation) can be activated in natural rocks and may lead to a deviation from pure solid-state models of rate-limiting deformation processes in quartz (Karato, 2008; Paterson, 2012). A detailed microstructural and chemical investigation has been carried out to document the grain boundary processes in experimentally deformed quartz aggregates to bridge this gap in our knowledge. The naturally occurring fine-grained novaculite employed in this study (Fig. 1) has a 2D grain size of 3.80 μm (3D mode = 5.70 μm). A similar range of sizes has been observed for dynamically recrystallized grains in an originally coarse-grained (~200 μm) Tana quartzite deformed in previous studies (Nègre et al., 2021; Pongrac et al., 2022). Thus, novaculite may be considered as an example of a completely recrystallized material generated from a former coarse grained natural quartzite. Consequently, using novaculite in experiments, it is possible to quantify the influence of grain size reduction by recrystallization of more than two orders of magnitude on the mechanical creep data. Such quantification allows us to estimate the strain weakening in the crust. Furthermore, we introduce an additional quartz flow law for the smaller grain size applicable to rheological modelling and a better understanding of shear zone processes.

2. Starting material and sample preparation for deformation

We used pure (>99 % silica), highly dense (without any visible porosity), fine-grained white Arkansas novaculite as starting material (Fig. 1). The sample orientation for the microstructural characterization of the starting material is the same as the cylindrical cores prepared for deformation experiments. All the cylindrical samples of 8 mm diameter were core-drilled from the starting material and dried at 110 °C for one day. In most cases, the central locations of samples that experienced the highest strain were analysed. We also checked the top part of the samples, located closest to the upper alumina piston, where far less strain was acquired. The thick sections were mechanically polished with the diamond paste of decreasing grain size (9, 3, 1, 0.25 μm), at least 10 min for each step. Once good surface conditions were achieved, final polishing with colloidal silica (0.04 μm) was carried out for 20 min. Microstructural and chemical analysis were performed from polished sections parallel to the long axis of the cores, using Scanning electron microscopy (SEM), Electron backscatter diffraction (EBSD), Electron probe micro-analyzer (EPMA) equipped with a cathodoluminescence (CL) detector and Secondary-ion mass spectrometry (SIMS). Please see supplementary text for more details.

The initial microstructure is very homogeneous, consisting of grains with straight grain boundaries and triple grain junctions indicating an equilibrium microstructure (Fig. 1a-c). A few sporadically distributed large quartz clasts up to ~100 μm in size are detected (Fig. 1a). The hyperspectral cathodoluminescence (CL) image (see supplementary text) shows largely yellow luminescence. The CL spectra shows a very prominent peak at 650 nm (Fig. 1d). Electron backscatter diffraction (EBSD) map (see supplementary text) shows that most of the grains are strain-free, i.e., without any internal misorientation (Fig. 1e). Only a few larger grains show some degree of intragranular misorientation, giving

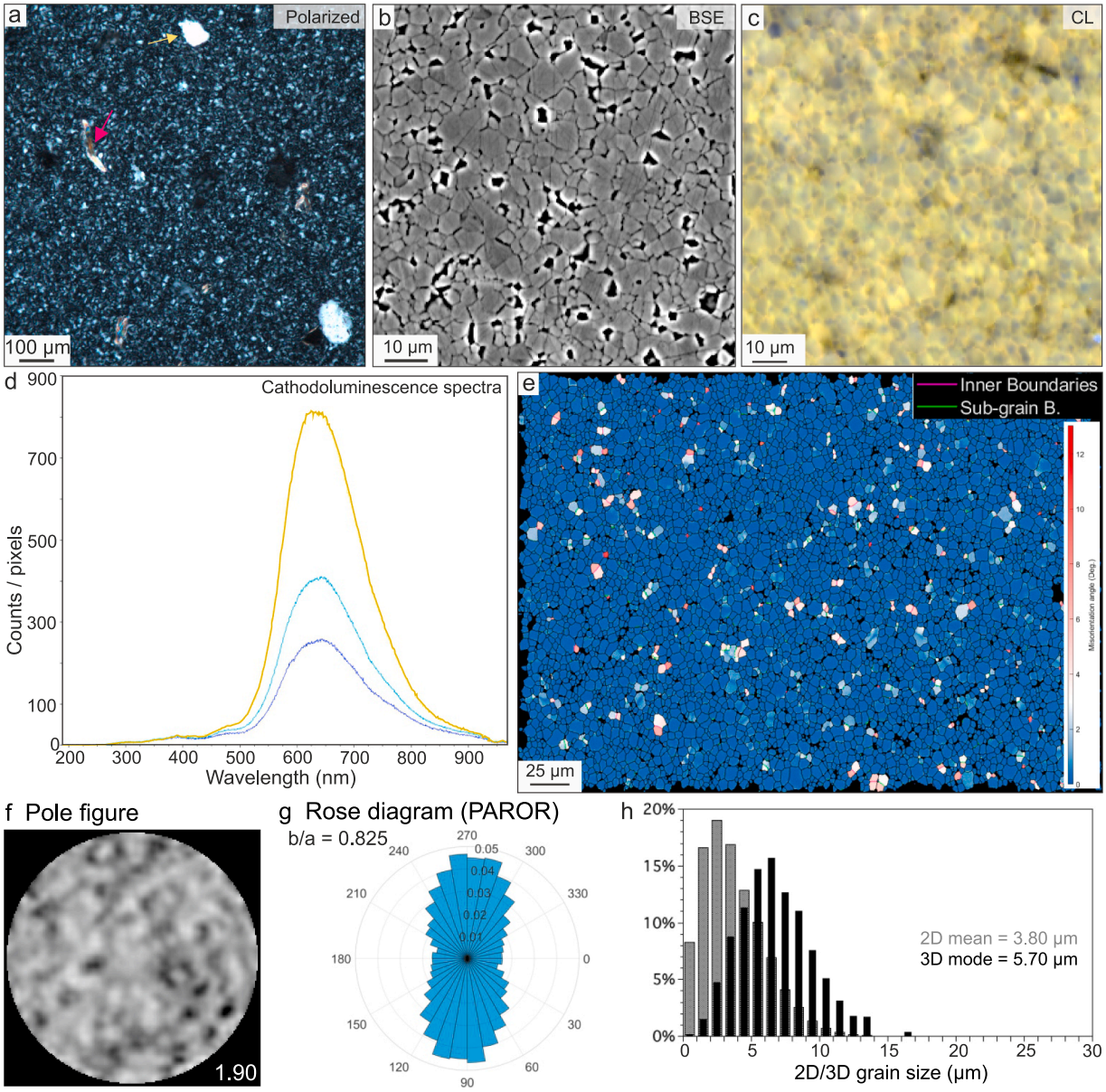

Fig. 1. Microstructural characterization of undeformed novaculite performed on a cylindrical core oriented parallel to the intended compression direction. a Cross-polarized light-microphotograph showing sporadically distributed large quartz clasts (yellow arrow) and micas (pink arrow). b BSE image that reveals a typical homogeneous microstructure. c Cathodoluminescence (CL) image that indicates a largely homogeneous initial colour spectrum of quartz grains. The corresponding spectra with a very prominent peak at 650 nm are shown in Supplementary Fig. 5. d CL spectra with a very prominent peak at ~650 nm corresponding to different luminescence (yellow to slightly blueish) seen in the previous CL map. A very subdue peak can be observed between 375 and 400 nm. **e** EBSD misorientation map showing grains mostly free of internal strain. Three types of boundaries are plotted: i) high-angle grain boundaries (black lines) defined by misorientation angle >10°, ii) low-angle boundaries defined by misorientations between 2 and 10°, including continuous sub-grain boundaries (green lines), and discontinuous inner boundaries (pink lines). Sub-grain boundaries form closed polygons, while inner boundaries do not. **f** Pole figure of the c-axis orientation highlighting no preferred orientation. **g** Quantified shape fabric in terms of particle ODF (PAROR) (ODF with maximum indicated on the figure, 10 contours 0.5 - 5.0) on a rose diagram (supplementary text). The bulk b/a is indicative of the shape anisotropy of the quartz grains. $b/a = 1$ indicates that the bulk shape of the particles is closer to a circle, while the lower values until '0' indicate a progressive increase in anisotropy. **h** Histograms of 2D and 3D grain size distribution of quartz grains.

rise to the development of low-angle boundaries. The crystallographic preferred orientation (CPO) of quartz considering the mean orientation of *c*-axes (Fig. 1f) confirms an initial random orientation. The bulk axial ratio $b/a = 0.825$ (long axis = *a*, short axis = *b*; Fig. 1f) indicates that the bulk shape of the grains is not equiaxed. The PAROR rose diagram (see supplementary text) shows that there is a shape preferred orientation (SPO) parallel to the cylindrical long axis (Fig. 1g). EBSD measurements of the mean 2D equivalent-diameter grain size is 3.80 μm (Fig. 1h). Although limited by the step size (0.2 μm) for lower values, such a 2D grain size of novaculite samples was also recorded in earlier studies (Fukuda et al., 2019; Kronenberg and Tullis, 1984; Tullis and Yund, 1982). The 3D grain size analysis (see supplementary text) shows a typical unimodal bell-shaped distribution with 3D mode of 5.70 μm (Fig. 1h). This value should be considered as the representative grain size. Minor secondary phases include mica and rutile, the former one being the source of additional H_2O and Al during the deformation (Supplementary Fig. 1). Point analysis (10 × 10 μm area) data by SIMS (see supplementary text) indicate that initial average H_2O content in quartz is 1270 H/10^6Si (measurements vary from 766 to 1954 H/10^6Si).

Four cylindrical samples were prepared for load-stepping experi-

ments in the new generation solid-medium (NaCl) Griggs apparatus (Orléans, France, Précigout et al., 2018) at a constant temperature of 900 °C and a confining pressure of 1 GPa (Fig. 2a, b). The 'as-is' sample (OR107) was prepared without adding water after drying at 110 °C for one day before weld-sealing the jacket (Fig. 2b). In the 'H_2O-added' sample (OR105), 0.1 wt.% of distilled water was added after drying at 110 °C for one day. The 'dry' sample (OR113) was prepared by drying novaculite at 300 °C for one day under atmospheric conditions. We also prepared a 'super-dry' sample (OR116) by drying it at 1000 °C for one day. In the 'dry' sample, we expect much of the adsorbed H_2O at surfaces to be removed in comparison to the 'as-is' sample, while H_2O at grain boundaries or within the crystal structure of quartz, or in the micas, remains intact. In contrast, the 'super-dry' sample is expected to have most of the H_2O removed from grain boundaries and crystal lattice in comparison to the undeformed novaculite (later, SIMS analysis also confirm this), in addition to decomposition of micas. One temperature-stepping experiment (OR111) was performed between 900 °C and 750 °C at constant load with the 'as-is' novaculite (Fig. 2c). The final microstructures from these stepping experiments are the result of complex $\sigma - \dot{\varepsilon}$ history that the sample experienced at different steps. Therefore, we carried out two additional constant-$\dot{\varepsilon}$ ($\sim 10^{-6}$ s^{-1}) H_2O-added and as-is experiments (689, 691) in a first-generation Tullis-modified Griggs apparatus (see Supplementary text) under the same P-T conditions (Fig. 2d) with slightly higher total strain than their counterpart load-stepping experiments for representative microstructural analysis corresponding to a constant $\dot{\varepsilon}$.

3. Results

3.1. Mechanical data

All our mechanical data were processed using a MATLAB program adapted by J. Précigout (www.jacques-precigout.fr). The shortening of the samples was determined from the instrument record considering the subsequent sample lengths at any given moment during the experiments. To calculate the $\dot{\varepsilon}$ out of load-stepping experiments (Fig. 2b), a straight line was fitted through the last part of the strain-time curve corresponding to the steady state condition (cf. Ghosh et al., 2022). Average σ-values (i.e., load/area) for each step were obtained from the steady-state portion of the mechanical record after correction of sample

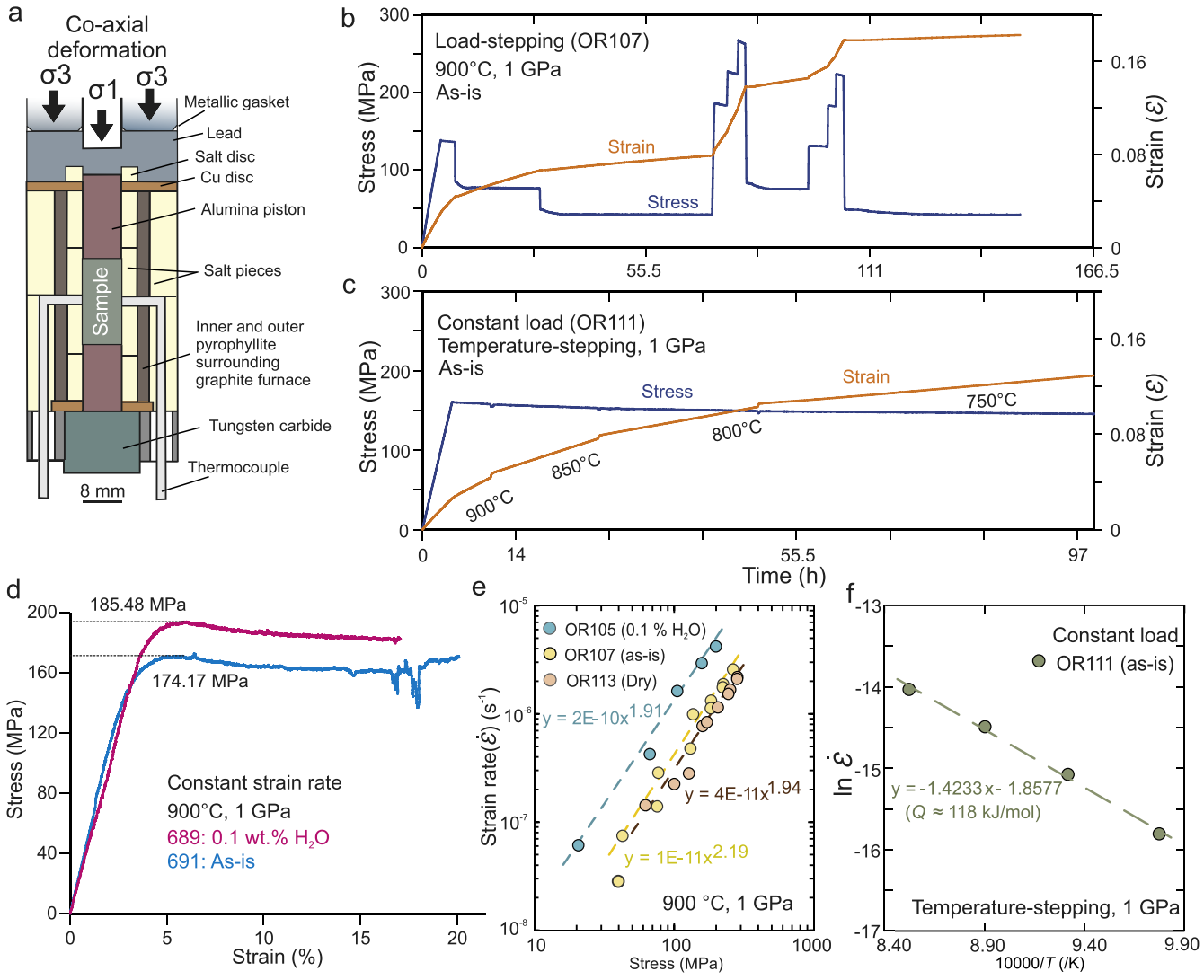

Fig. 2. Experimental setup and Mechanical data. a Schematic diagram of the coaxial experimental set-up in the new generation Griggs apparatus. **b** A typical stress-strain-time data (OR107) obtained during load-stepping experiment at 900 °C and 1 GPa. **c** A typical stress-strain-time data obtained during temperature-steeping (900 to 750 °C) at constant load and 1 GPa confining pressure (OR111). **d** Stress-strain curves for constant strain rate experiments. σ and $\dot{\varepsilon}$ values are calculated from the peak strength portion of the mechanical curve. **e** Determination of stress exponent (n) in a log-log space from load-stepping experiments (as-is, H_2O-added, and dry). The slope of the global fit indicates the n-value. **f** Arrhenius plot for the determination of the activation energy (Q) using the as-is constant-load experiment.

shortening and rig stiffness. Differential stress was calculated as $\Delta\sigma = \sigma_1 - \sigma_3$, based on the definition of the conventional hit point (Holyoke and Kronenberg, 2010). As expected, strain increases faster with increasing load on the sample (supplementary Fig. 2) and the slopes of the strain-time curves need some time to attain a steady state condition. At the highest *T*-step of the constant-load experiments (Fig. 2c), the overall slope of the strain curve is slightly convex, while it becomes slightly concave at the lowest *T*. The σ values also decreased slightly (~10 MPa) with time as a consequence of the increase in the surface area of the deformed sample (as the load is constant). Depending on the number of steps and $\dot{\varepsilon}$ at each step, the bulk strain in our experiments ranges up to a maximum value of ~21.3 %. Experimental conditions and the corresponding results are sequentially shown in Table 1.

During the constant-$\dot{\varepsilon}$ experiments, stress-strain curves were generated for the as-is and 0.1 % H_2O-added samples that exhibits same mechanical behavior (Fig. 2d). After reaching the peak-stress, both stress-strain curves show slight weakening. The difference in flow stresses between the as-is and H_2O-added sample is within the expected variation of individual samples given an error of ±30 MPa for the Tullis-modified Griggs-type apparatus (Holyoke and Kronenberg 2010).

3.2. Determination of n and Q

σ and $\dot{\varepsilon}$ for the load-stepping experiments were plotted in a log-log space to calculate the *n*-value (Fig. 2e). The slope of the power-law-fit indicates *n*-values of ~1.91 for H_2O-added, ~1.94 for dry and ~2.18 for the as-is sample. However, if we do not consider the lowest stress point for the as-is experiment, then the *n* value becomes ~1.99. A similar issue with the lowest stress data was noted earlier (Ghosh et al., 2022). Given the ± 30 MPa accuracy of the solid-medium apparatus (Holyoke and Kronenberg, 2010), it is possible that such low stress values are less reliable. The *T*-stepping data are plotted in the Arrhenius $ln(\dot{\varepsilon}) - T^{-1}$ space (Fig. 2f). $Q = 118$ kJ/mol was determined from the slope of the global fit in the Arrhenius space, independent of the *n*-value. The *n* and *Q* values measured from the novaculites are similar to those obtained from the coarse-grained Tana quartzite (Ghosh et al., 2022).

3.3. Microstructural observations

The misorientation images from the two constant-$\dot{\varepsilon}$ samples show the formation of distorted crystal structures in the quartz grains, giving rise to the development of low-angle inner boundaries (marked in pink) and discrete sub-grain boundaries (marked in green) (Fig. 3a, b). The grain size distribution (GSD) remained 'broadly' unimodal with slight increase in $d_{3D\ (mode)}$ (Fig. 3c) in comparison to the pre-deformed value (Table 1). Interestingly, the original SPO (Fig. 1h) has been replaced in the deformed samples and the grains tend to align with their long axis perpendicular to the compression direction (Fig. 3c). The lower values of the bulk axial ratio ($b/a \approx 0.65$) compared to the pre-deformed value (Fig. 1h) suggest that the grains were flattened. The corresponding CPO strengths remains weak without any significant CPO pattern development (Fig. 3c). Both constant-$\dot{\varepsilon}$ samples reveal a comparable microstructure in CL and element maps. Three types of domains are visible and distributed in a patchy way: (i) domains with aggregates of CL-yellow grains, (ii) domains where CL-yellow grains are less abundant, and grains with CL-yellow cores surrounded by a CL-dark luminescence, and (iii) domains where grains with CL-yellow cores surrounded by a CL-blue luminescence. The CL-yellow grains have on average a lower Al^{3+}

Table 1
Summary of the experimental results.

Experiment	*T* (°C)	H_2O (wt.%)	Height (mm)	σ (MPa)	$\dot{\varepsilon}$ (s^{-1})	Duration (hr)	Final ε (%)	$d_{2D(mean)}$ μm*	$d_{3D(mean)}$ μm
OR105	900	0.1	15.03	105.08	1.63E-06	~27.88	11.67	6.40	10.20
				157.54	2.95E-06				
				198.75	4.19E-06				
				20.56	6.11E-08				
				66.82	4.24E-07				
OR107	900	as-is	15.01	136.55	9.94E-07	~148.55	18.26	6.50	12.6
				76.82	2.86E-07				
				42.59	7.49E-08				
				183.67	1.33E-06				
				224.40	1.89E-06				
				263.37	2.57E-06				
				75.31	1.40E-07				
				130.61	4.78E-07				
				182.39	1.13E-06				
				222.16	1.76E-06				
				42.33	2.91E-08				
OR113	900	dry	15.02	62.17	1.43E-07	~149.61	21.30	6.20	11.8
				159.43	7.72E-07				
				205.44	1.15E-06				
				100.10	2.25E-07				
				251.96	1.67E-06				
				127.28	2.82E-07				
				244.21	1.53E-06				
				283.00	2.19E-06				
				171.51	8.39E-07				
				282.73	2.10E-06				
OR116	900	super-dry	14.77	–	–	~196.20	–	4.06[$]	6.22[$]
OR111	900	as-is	14.98	158.79	8.04E-07	~198.47	18.52	–	–
	850			154.86	5.09E-07				
	800			150.35	2.83E-07				
	750			146.86	1.36E-07				
689	900	0.1	12.71	185.48[#]	1.18E-06	~39.86	16.50	3.74	6.18
691	900	as-is	12.73	174.17[#]	1.31E-06	~43.66	20.30	3.72	6.41

[*] Initial grain size is 3.80 μm in 2D and 5.70 μm in 3D. The 2D mean grain sizes are shown to have parity with the previous studies. The 3D mode can be found in the histograms.

[#] Peak stress values are shown.

[$] For the 'super-dry' sample the initial undeformed grain size after annealing and the final deformed grain size does not show any variation.

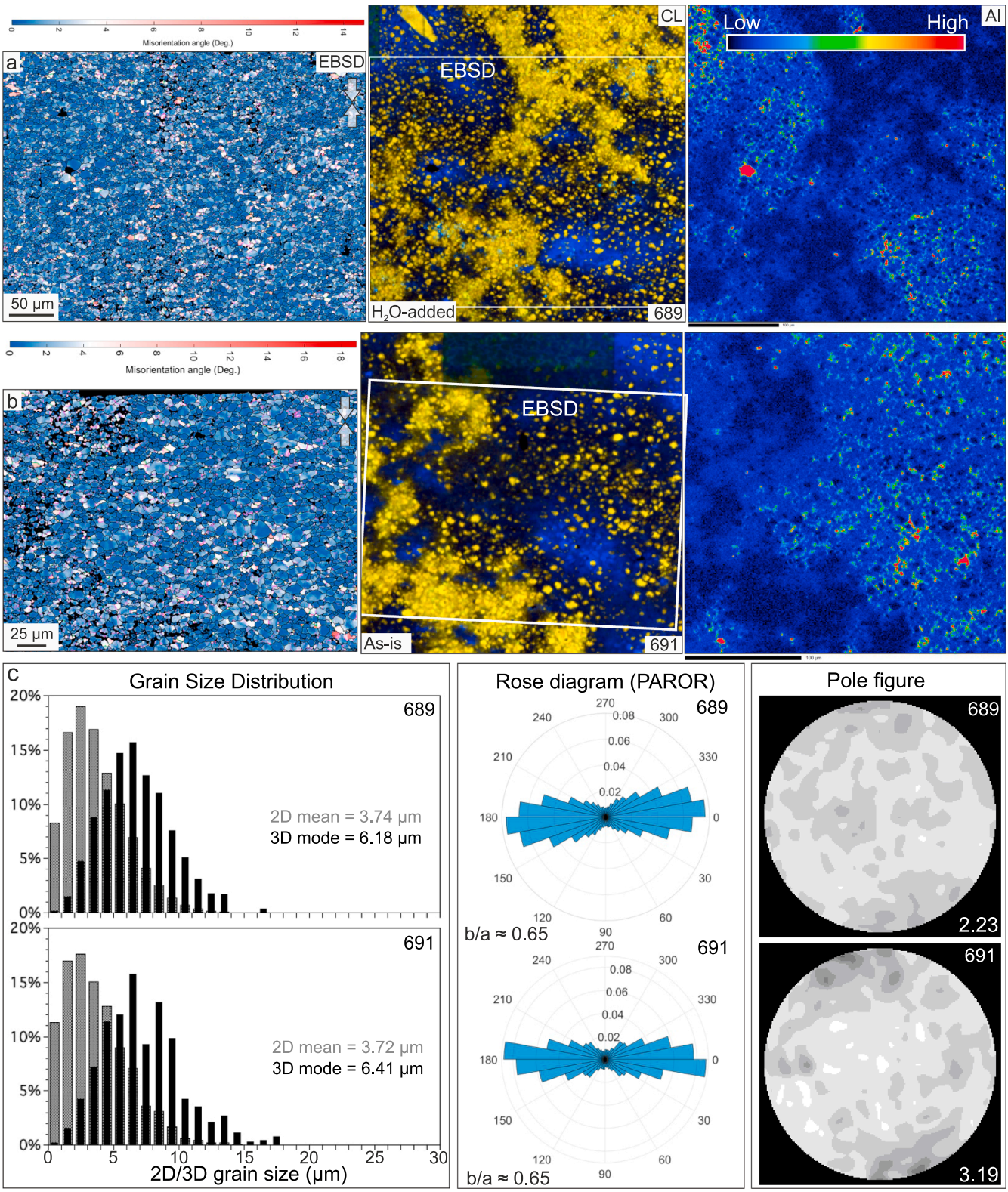

Fig. 3. Microstructural and chemical observations from the central portion of the as-is (691) and 0.1% H_2O-added (689) samples deformed under constant $\dot{\varepsilon}$. The long axis orientation (i.e., compression direction) of the cylindrical novaculite cores is vertical (white arrow). **a-b** The locations of the EBSD maps are marked as white box on the CL figures. Intragranular misorientations ("mis2mean" function in MTEX) of quartz grains are shown. Slightly finer grains corresponding to the CL-yellow areas correspond to non-indexing problem in the EBSD maps. The corresponding Al map shows a positive correlation with the CL colours. Also, see Supplementary Fig. 6 corresponding to a different location from H_2O-added sample. **c** The 3D grain size distribution (GSD) remains 'broadly' unimodal. Pole figures of the *c*-axis orientation show random fabric (ODF with maximum indicated on the figures, 10 contours 0.5 - 5.0). The PAROR rose diagram shows the development of a strong SPO in the deformed samples.

content than domains with CL-blue and CL-dark luminescence (Fig. 3a, b). The CL blue and dark zones visually contain slightly coarser grains than the CL-yellow zones. From the EBSD maps of the load-stepping samples (supplementary Fig. 5a-e), the as-is and dry samples revealed that some areas patchily show grain coarsening in contrast to the H_2O-added sample with more or less homogeneous GSD (supplementary Fig. 5f-h). In Fig. 4 and Supplementary Fig. 4, the corresponding back-scattered electron (BSE), CL, and element maps from the load-stepping samples are shown. The as-is and dry samples showed regions of grain coarsening, which correspond to different orders of blue luminescence (darker to brighter) with a similar spectral pattern (Fig. 5). In contrast, the areas retaining finer grains typically show yellow luminescence. A

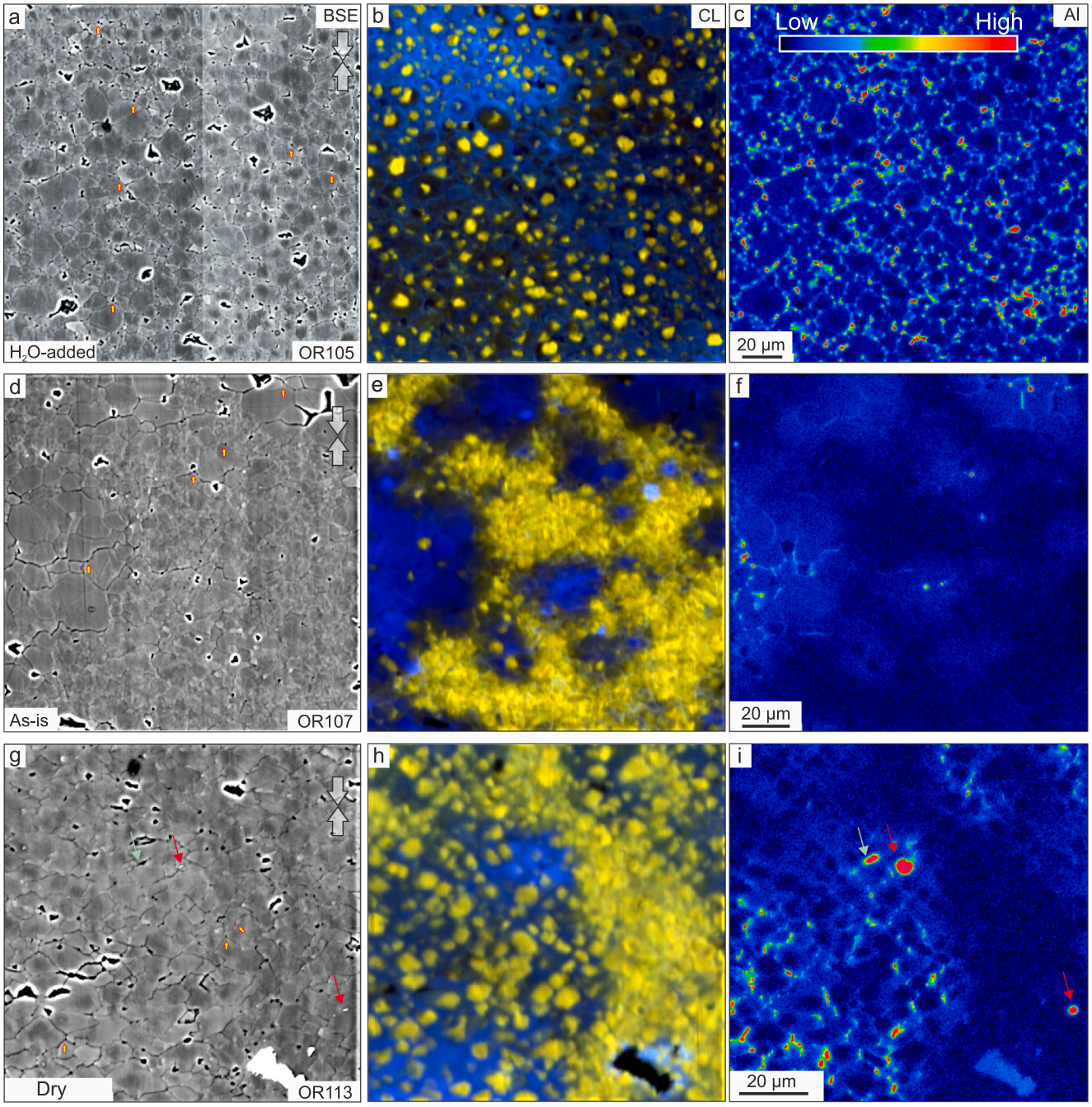

Fig. 4. Microstructural and chemical observations from the central portion of the samples deformed under constant load. a-c Deformed H_2O-added sample that shows a homogeneously dispersed core-shell microstructure (b) and grain size distribution (a). A third darker luminescence (b) is better observed between the bright blue and yellow color in CL within individual grains. Notice that the CL-yellow or the Al-poor (c) cores are of different sizes and not always located at the centre of the individual grains. BSE image shows that the porosity (yellow arrow) is pervasively developed through the sample. **d-f** Deformed as-is sample shows patchily developed CL-blue (e) that generally correspond to the larger grains (d) with higher Al content (f). Inside of a few grains, the original CL-yellow luminance was preserved which forms the core-shell microstructure of individual grains. Porosity is not developed in the zones containing finer grains (~ CL-yellow) with low Al content. **g-i** Deformed dry sample that shows a significant portion of the image where the finer grains correspond with CL-yellow luminescence (h). In comparison to the as-is sample, the CL-yellow zones witnessed some porosity development. The bright phases (with high Ti content) marked by the red arrow and the open grain boundaries marked by the green arrow in BSE (g) are exaggerated by the red color in WDS (i). Larger holes represent plucked grains from sample preparation. Further information about microstructural and chemical features of the deformed samples are also available in supplementary Figs. 4 and 5.

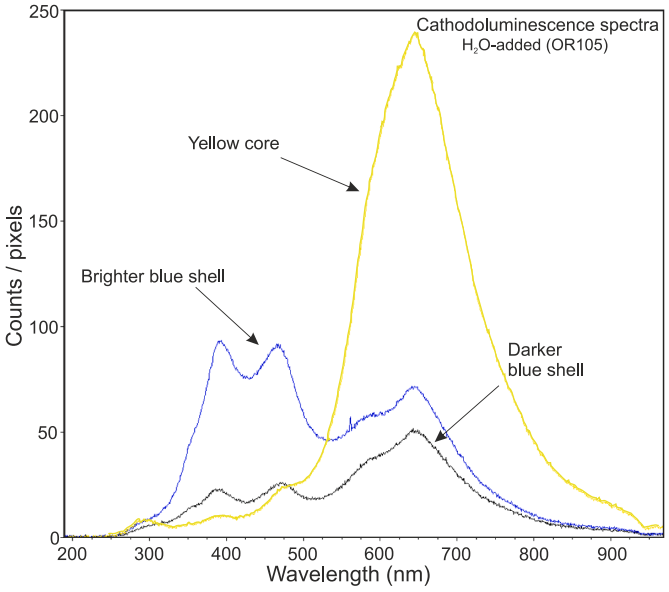

Fig. 5. Typical CL spectra of core-shell structures in the H_2O-added sample. While the reconstituted brighter blue shell shows a similar spectra pattern (with new prominent peaks between 350 and 475 nm) as the darker blue shell, the yellow core shows a very prominent peak at 650 nm, similar to the undeformed novaculite as shown in Fig. 1d.

closer inspection reveals that some of the coarser grains contain a yellow core surrounded by a darker shell, which progressively becomes brighter blue towards the grain boundary. In contrast to these samples, the H_2O-added deformed sample show more homogeneously developed core-shell structures. The individual core-shell structures are not always symmetric with respect to the grain boundaries and cores possess a sharp polygonal shape (Supplementary Fig. 4b). A similar homogeneously-developed core-shell can be observed in the H_2O-added constant-$\dot{\varepsilon}$ sample (689), but from a different location (Supplementary Fig. 6).

The CL spectra corresponding to three different luminescence that constitutes a core-shell structure in the H_2O-added sample is shown (Figs. 5, 6a). The brighter blue silica material shows a similar spectral pattern as the darker blue shell, but the two prominent wavelength peaks between 350 and 475 nm are more intense for the brighter blue shell. On the contrary, the yellow core shows a similar pattern as the undeformed novaculite (Fig. 1d) with a very strong peak at 650 nm. It is clear from the element line profile that the yellow cores become brighter blue as the Al^{3+} content increases from the core to the boundary (Fig. 6a). The grain boundary regions are highlighted by elements such as Al, Ca, K and Na (Fig. 6b, Supplementary Fig. 4 h) and a positive correlation is found between the Al^{3+} versus Na^{+} and K^{+} from the line profiles within the quartz grains (Fig. 6c). SIMS point analysis data from all the samples indicate a positive correlation between $H/10^6Si$ and $Al/10^6Si$ (Fig. 6d). Both the as-is and H_2O-added samples do not show significant differences in terms of grain-scale H_2O content. The lowest values of point analysis data from the interiors of the deformed grain should overlap the values measured from undeformed quartz aggregate. However, due to large spot size (~10 μm) the grain interior values have some contribution from the shells. Interestingly, the as-is quartz aggregate contains a much higher amount of H^{+} than the source novaculite, indicating additional amount of H_2O released from the micas during deformation. SIMS point analysis data indicate low average H_2O contents of 454 $H/10^6Si$ (varies from 399 to 472 $H/10^6Si$) in the super-dry sample.

The BSE and band contrast images from the deformed samples commonly show many grains with straight boundaries and triple (some quadruple) junctions and new porosity development along those junctions and grain boundaries (Figs. 4a, d, g, 6e-g). Some of the small pore spaces show high Al-contents in the WDS maps (Fig. 4a, c). Such red spots often are exaggerated in size as a consequence of analytical resolution. However, the pore spaces and boundaries can act as reservoirs for the fluid and the elements dissolved in it. It is noteworthy that a few grain boundaries from the H_2O-added sample (Fig. 6e) are curved (marked by a green arrow) in the BSE maps. This feature is typically observed in natural samples with grain boundary migration (GBM) (Stipp et al., 2004).

The core-shell structure indicates that there was a progressive reconstitution of silica material from the core to the boundary, which can be detected by CL. It is well known that the top part of the deformed samples, closest to the alumina piston, acquires far less strain than the central part. The EBSD map shows evidence of minor internal crystal-plastic deformation and the development of a weak SPO (Fig. 7c). Additionally, it is clear that far less grain boundary reconstitution and porosity development (Fig. 7a, b) had occurred in comparison to the microstructures in the more deformed parts. The 'super-dry' sample is too strong to be deformed under differential stresses (as high as > 900 MPa) below the confining pressure. It is also clear from the EBSD maps that there is no internal crystal-plastic strain and grain sizes did not show any significant modification (Supplementary Fig. 7). CL maps indicate that no grain boundary reconstitution had occurred (Fig. 7d).

4. Discussion

4.1. Comparison with previous studies

Using the 0.1 wt.% H_2O-added coarse-grained quartzite (Tana quartzite) flow law (Ghosh et al., 2022) with $n = 2$ and $Q = 110$ kJ/mol (Eq. (2)), the $\dot{\varepsilon}$ values are calculated at the σ, T, and P reported (Table 1) from individual novaculite experiments. These $\dot{\varepsilon}$ values (transparent circles) and the red line derived from the Eq. (2) are shown in Fig. 8a-d. The H_2O-added novaculite is ~ 3.5 times weaker than the as-is novaculite (Fig. 8a, b). A similar strength difference (~ 4 times) has been observed between the 0.1 wt.% H_2O-added and as-is Tana quartzite (Ghosh et al., 2022). The as-is novaculite is ~ 4.5 times weaker than the as-is Tana quartzite (Fig. 8a). The H_2O-added novaculite is ~ 4 times weaker than the H_2O-added Tana (data calculated from the flow law, Eq. (2)) at the same condition (Fig. 8b). The dry and as-is novaculite samples show only slight (~ 1.4 times) differences (Fig. 8c). The maximum strength difference (more than an order of magnitude) arises between the end-member samples, i.e., the as-is Tana and H_2O-added novaculite, where the combined effect of grain size and addition of H_2O accumulates. The activation energy for as-is novaculite calculated from the Arrhenius $ln(\dot{\varepsilon}) - T^{-1}$ space is very similar to the values calculated from the Tana quartzite (Fig. 8d). Thus, the slope of the creep data (log-log and Arrhenius space) indicative of n (= 2) and Q (= 110 kJ/mol) values does not change between the novaculite (as-is, H_2O-added, and dry) and Tana samples (as-is and H_2O-added) within the error associated with the Griggs apparatus. Therefore, the strength difference between these experiments is best expressed by the different A-values of the flow law (see supplementary text). For example, multiplication of the A-value (Eq. (2)) with 3.5 predicts the strength of the 0.1 wt.% of H_2O-added novaculite.

In Fig. 8e, the original mechanical data (σ and $\dot{\varepsilon}$) were normalized to the non-dimensional stress (σ_0) and strain rate ($\dot{\varepsilon}_0$) ratios in reference to the coarse-grained Tana flow law (Eq. (2)). In this way, we can compare the results from earlier constant-$\dot{\varepsilon}$ experiments using the novaculite and coarse-grained quartzite, where mechanical data were obtained from a variety of σ, $\dot{\varepsilon}$, T, and P conditions (Ghosh et al., 2021; Yabe et al., 2020). Only the results from previous studies that satisfied the Goetze's criterion were used to avoid any contribution from the brittle deformation mechanisms. The original mechanical data (σ and $\dot{\varepsilon}$) published earlier was normalized to non-dimensional stress (σ_0) and strain rate ($\dot{\varepsilon}_0$) ratios as $\sigma_0 = \frac{\sigma}{\sigma^{*ref}}$ and $\dot{\varepsilon}_0 = \frac{\dot{\varepsilon}}{\dot{\varepsilon}^{*ref}}$. Here, the reference strain rate ($\dot{\varepsilon}^{*ref}$) was

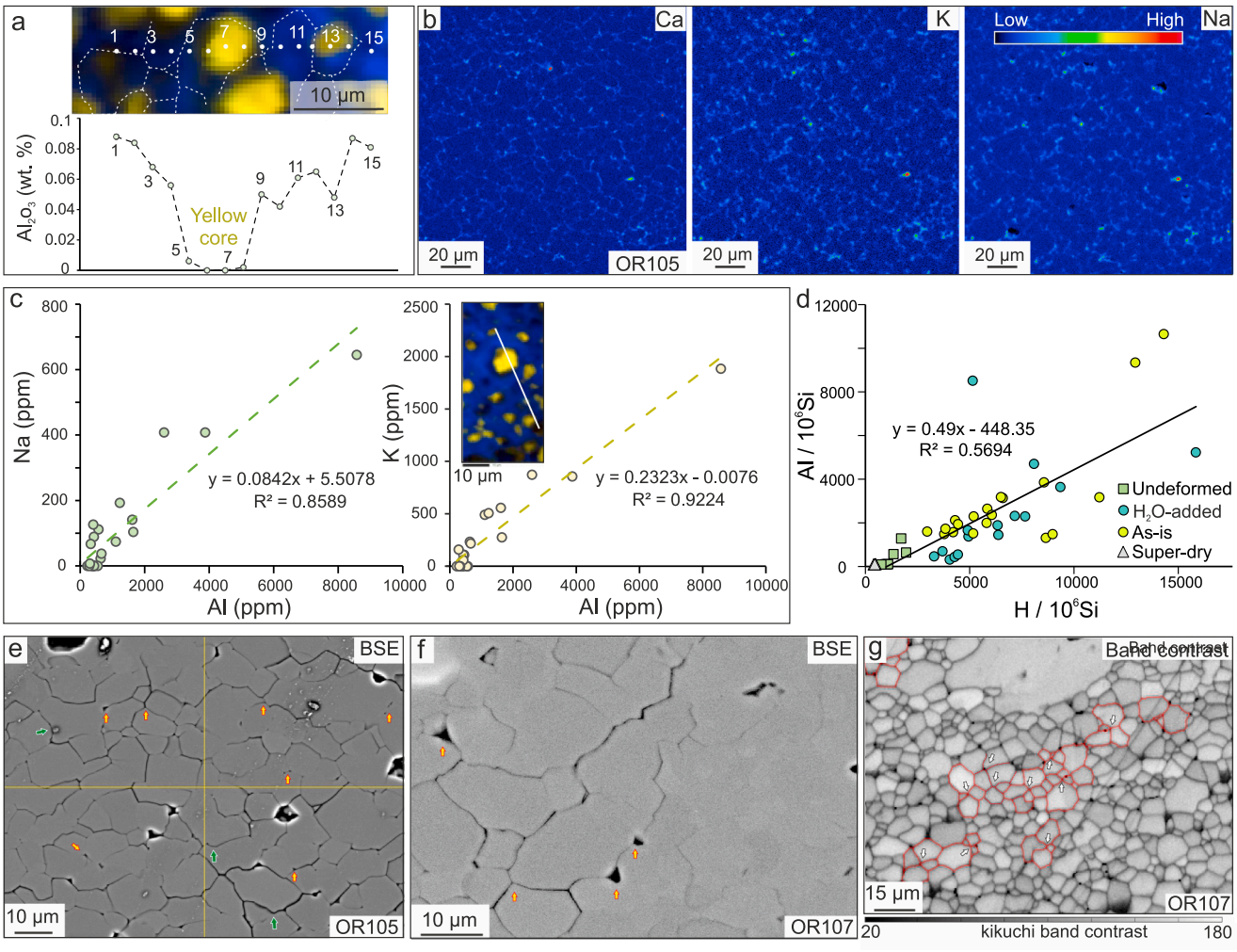

Fig. 6. Microstructural and chemical observations from the central portion of the deformed and undeformed novaculite samples. a Al content across several quartz grains with different CL luminescence using EPMA point analyses. The inset CL image is taken from the H_2O-added deformed sample shown in supplementary Figure 4b. **b** Map distribution of Ca, Na, and K in a representative area of the H_2O-rich deformed sample. Grain boundaries are highlighted by element concentrations along them. **c** Na^+ and K^+ versus Al^{3+} in quartz grains across an EPMA line transect located on the CL map of the H_2O-added deformed sample. **d** Al versus H (normalized to 10^6Si) of quartz grains in all samples using SIMS point analyses. This graph indicates a positive correlation between H/10^6Si and Al/10^6Si. Notice the original undeformed novaculite is dried at 110 °C for one day. **e and f** BSE images of representative areas in the H_2O-added sample. They highlight a porosity development along grain boundaries and junctions (yellow arrows), as well as curved grain boundaries (green arrows) that are indicative of grain boundary migration (GBM). **g** EBSD band contrast map of a representative area in the as-is sample. The map documents grain boundaries (red lines plotted using MTEX) with unequivocal presence of four-grain junctions (white arrows), commonly indicative of grain boundary sliding.

calculated from the Tana flow law (equation 2) by substituting the T with temperature-values at which each original mechanical data was acquired and the stress term (σ) with the σ^{*ref}. A fixed value of 100 MPa as $\dot{\varepsilon}^{*ref}$ was used in this calculation. The strength differences between the Tana quartzite and novaculites remain the same as those described in the previous section. Irrespective of the total strain, all the co-axial experimental data (as-is to H_2O-added) from earlier natural coarse-grained samples are plotted in the shaded region (cf. Ghosh et al., 2022). The as-is novaculite deformed at 700–850 °C and 1 GPa (Bishop, 1996) followed our as-is novaculite results at higher σ and $\dot{\varepsilon}$. H_2O-added (0.03 to 0.4 wt.%) novaculite deformed at 800 and 850 °C (Kronenberg and Tullis, 1984) plot between our as-is and H_2O-added novaculite data demonstrating a good reproducibility for similar starting material. These observations confirm the capability of the coarse-grained Tana flow law (Eq. (2)) to express the original mechanical data in a predicted manner from previous studies using novaculite, given $a \pm 30$ MPa error generally associated with the Tullis-modified Griggs-type apparatus (Holyoke and Kronenberg, 2010). It is not surprising that the 0.2 wt.% H_2O-added mixture of coarse- and fine-grained quartz aggregate made from pulverized dry single crystal of quartz (Richter et al., 2018) is following the trend of our as-is novaculite and H_2O-added Tana quartzite data, but at higher σ and $\dot{\varepsilon}$. Richter et al. (2018) also documented $n = 1.8$, which again confirms that the n-value is rather grain-size-insensitive. Furthermore, the data from the coarse-grained (~100 μm) Black Hills quartzite (Heilbronner and Kilian, 2017; Kidder et al., 2016; Stipp et al., 2006) fall between our end-member data, that is as-is Tana and H_2O-added novaculite. The mechanical data from these studies were chosen as they clearly document significant recrystallization. Mechanical data from fine-grained quartz-sand power (Fukuda et al., 2018), using the Tullis-modified Griggs apparatus forms the upper boundary of the shaded region in the nondimensional plot. Interestingly, they also recorded a n-value close to 2 (~1.8). These data are weaker than our H_2O-added novaculite, although the difference is not large. This may reflect the inherent variability between starting materials. Although, Rutter and Brodie (2004b) reported grain-size-sensitive diffusion creep ($n = 1$) from extremely fine-grained quartz aggregates, their data broadly overlap our data. This is surprising, given that GSS creep is supposed to significantly weaken the samples. Nonetheless, our

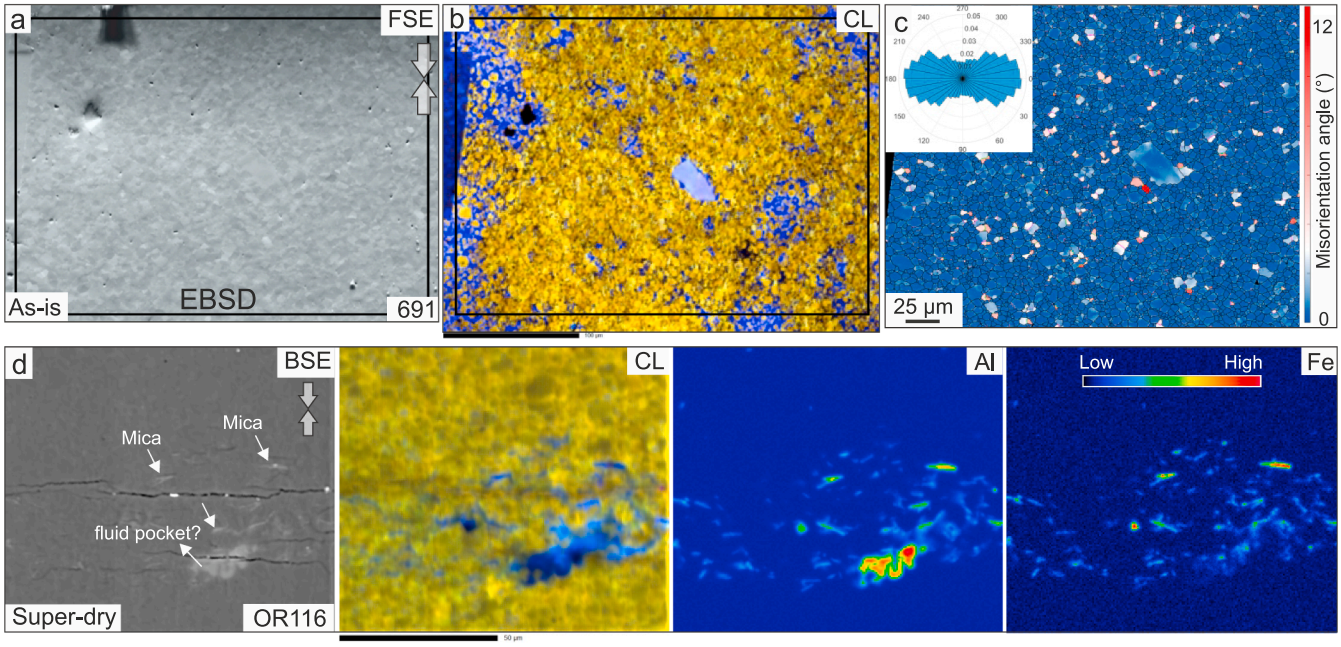

Fig. 7. Microstructural and chemical observations of the as-is and deformed samples. a Forescattered electron (FSE) image from the top portion of the as-is (constant-$\dot{\varepsilon}$) sample. A very restricted porosity development is observed. **b** Corresponding CL map that shows a very limited reconstitution of grain boundaries in comparison to the microstructural observations described in Figs. 4 to 6. **c** Corresponding EBSD map of intragranular misorientations, which give rise to limited internal crystal-plastic deformation, although PAROR analysis indicates the development of a weak SPO. **d** BSE and CL images, as well as distribution of Al and Fe in a representative area of the super-dry deformed sample. In contrast to the other experiments (as-is, H_2O-added, and dry), the super-dry sample retains most of the original CL-yellow luminescence. We also observed fluid (melt?) pockets and mica-rich zones in contrast to other deformed samples.

novaculite results support their conclusion that diffusion creep does not dominate quartz at a grain size > 1 µm under the laboratory $\dot{\varepsilon}$.

4.2. CL-blue luminescence and substitution of Si^{4+}

Substitution of Si^{4+} by Al^{3+} is common in natural quartz, and leads to the joint incorporation of monovalent ions in the crystal structure for charge balance (Yuan et al., 2023). The CL-blue luminescence in quartz was shown earlier to contain high concentrations of Al^{3+} (Raimbourg et al., 2021) from natural samples. In the present study, the blue (dark to bright) CL signal from the deformed novaculites is also strongly correlated with Al^{3+}. On the other hand, if Ti^{4+} is present in the system, it can be also responsible for a blue luminescence (Bestmann and Pennacchioni, 2015). In the deformed novaculites, Ti^{4+} is present in very low concentration and found to be correlating with H^+ (see Supplementary text), but the corresponding CL-wavelength with a maximum at ~415 nm (Bestmann and Pennacchioni, 2015) is missing. Thus, it appears that Al^{3+} is responsible for the CL-blue spectra in our samples (Fig. 5), but future studies are needed to evaluate the effect of Ti^{4+} as it is also available in the novaculites. We found that Al^{3+} has a positive correlation with the monovalent cations (Na^+, K^+, H^+) for charge balance (Fig. 6c, d). It is likely that the grain boundaries together with opening and closing of pores (Fusseis et al., 2009) acted as fluid pathways for the transport of dissolved elements that may originate from impurities (e.g., micas) present in the novaculite. The $Na+K/Al$ atomic ratios vary up to 0.56 and the charge deficit possibly is compensated by the intake of H^+ (Perny et al., 1992; Stünitz et al., 2024). However, Al/H atomic proportion is of the order 0.5, which indicate H^+ is incorporated in larger proportion than what is needed for charge compensation. The high H^+ content might result from submicron size inclusions or H_2O present in the grain boundaries. Noticeably, the variation in the Al^{3+} content does not always correlate systematically with darker or brighter blue CL-luminescence (Fig. 6a). It is possible that charge-compensating ions are playing a critical role as the CL-activator (Fig. 5); the ions with larger atomic radius will distort the crystal lattice in comparison to the smaller ions (Yuan et al., 2023). The role of the individual charge-compensating cations on the CL signal is difficult to determine and needs further studies.

4.3. Deformation mechanisms related to grain boundary processes

The core-shell-structure observed under the CL implies a reconstitution process where the unaltered yellow core of the original grains is preserved and surrounded by reconstituted silica material that has exchanged elements while forming the shell. In the presence of an aqueous fluid along the grain boundaries, a GBM process takes place through dissolution-precipitation between adjacent grains (Fig. 9) (Pearce and Wheeler, 2010; Poirier and Guillopé, 1979; Urai et al., 1986). We can reasonably predict that the cations (Al^{3+}, Na^+, K^+, Ca^{2+}, H^+) present in the system can move by diffusion in the grain boundary fluid and that diffusion in the fluid is sufficiently fast to account for the concentration observed at the grain boundaries (Fig. 6b). Al^{3+} is incorporated into the quartz via exchange by the migrating grain boundaries, and the outer shell acquires a higher concentration of Al^{3+} and other monovalent cations required for charge balance (Fig. 6a). The volume of the altered composition (blue or dark shell) marks the local extent of the GBM process. A potential Al self-diffusion in SiO_2 is too slow to produce the width of the Al-enriched outer rims we observed (Tailby et al., 2018).

Our microstructural observations, such as the formation of pores, triple and quadruple junctions, straight boundaries, and the development of strong SPO along with change in shape of individual grains without any significant CPO (Fig. 3), are consistent with GBS-related processes observed in natural and experimentally deformed samples (Dimanov et al., 2007; Fusseis et al., 2009; Menegon et al., 2015; Rybacki et al., 2003; White et al., 1980). The efficiency of GBS can be increased by dissolution-precipitation in the following two ways: (1) GBM through dissolution-precipitation can modify the geometry of the grain boundary interfaces and orient the neighbouring grains plastically compatible for sliding (shape change). (2) The surface asperities (e.g.,

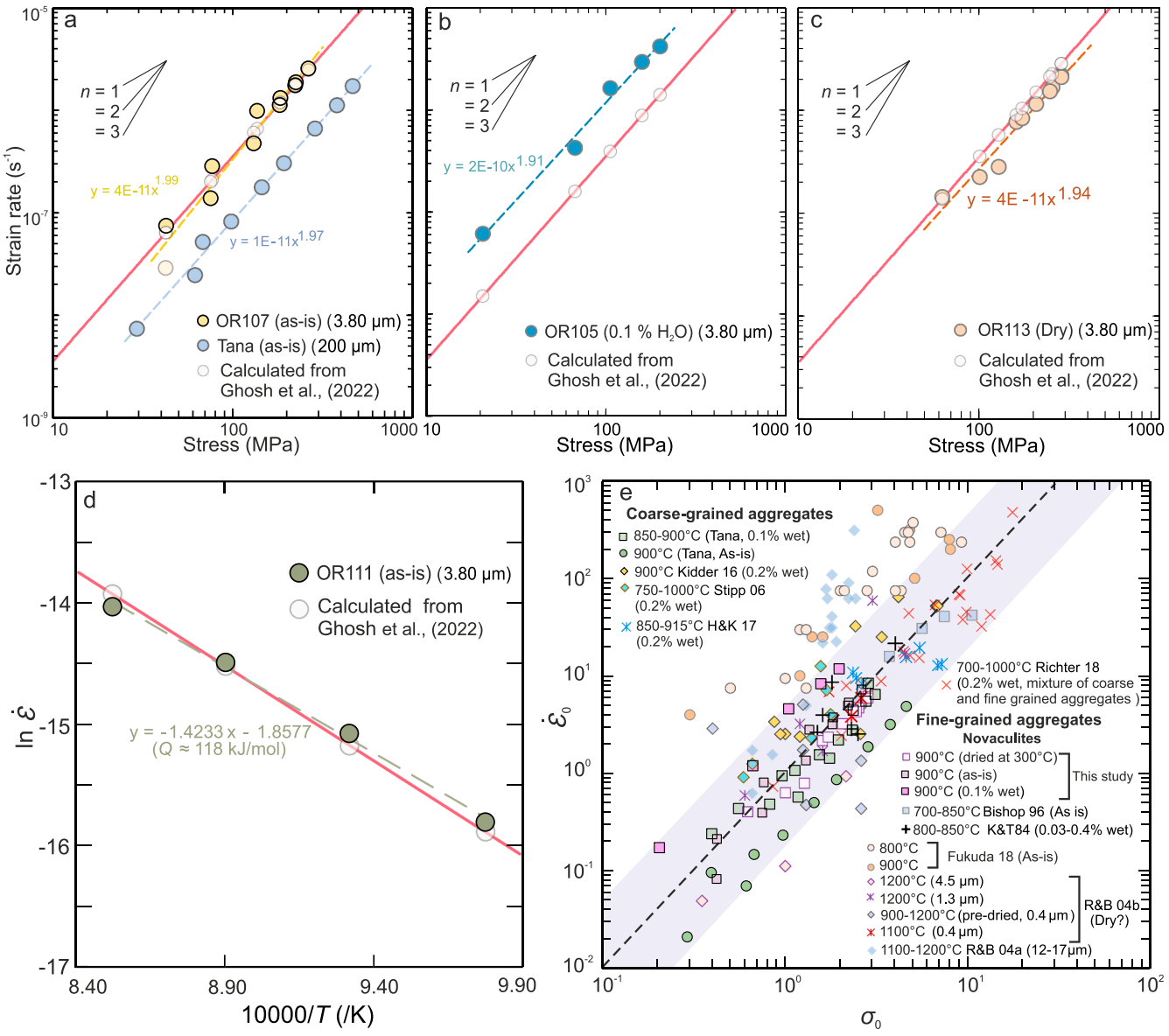

Fig. 8. Comparison of the mechanical data (σ and $\dot{\varepsilon}$) with previous studies. The red lines and the transparent data points are calculated using the coarse-grained, 0.1 wt.% H_2O-added Tana flow law (Eq. (2)) (Ghosh et al., 2022). **a** Log-log graph of stress versus strain rate of the as-is novaculite samples. The as-is novaculite is ~ 4.5 times weaker than the as-is Tana quartzite, but shows a similar stress exponent ($n \approx 2$). Notice that if we do not consider the lowest stress point for the as-is novaculite experiment, then the n-value becomes ~1.99 from a value of 2.19 (Fig. 2d). **b** Log-log graph of stress versus strain rate of the H_2O-added novaculite sample. The latter is here documented as ~ 4 times weaker than Tana quartzite based on the flow law from Ghosh et al. (2022). **c** Log-log graph of stress versus strain rate of the dry novaculite sample. In this case, the novaculite is slightly (~ 1.4 times) stronger than Tana quartzite considering Eq. (2). **d** In the Arrhenius $ln(\dot{\varepsilon}) - T^{-1}$ space, the data from as-is novaculite is similar to the values calculated from the Tana flow law. **e** Non-dimensional plot of strain rate ($\dot{\varepsilon}_0$) versus stress (σ_0) compiling the original mechanical data (σ and $\dot{\varepsilon}$) reported in the literature: Kronenberg and Tullis (1984; K&T84); Heilbronner and Kilian (2017; H&K 02); Rutter and Brodie (2004a and b; R&B04a,b); Stipp et al. (2006; Stipp 06); Kidder et al. (2016; Kidder 16); Fukuda et al. (2018; Fukuda 18); Richter et al. (2018; Richter 18). Only the results that satisfy the Goetze criterion have been included. Most of the creep results obtained from previous coarse- or fine-grained quartz aggregates overlaps with or follow our novaculite and Tana quartzite datasets, even the absolute strengths are essentially comparable (within a factor of ~5 times the $\dot{\varepsilon}$, indicated by the shaded region drawn from Fig.7a of Ghosh et al., 2022).

non-planar boundaries) can be removed by preferential dissolution and transfer of silica material over a short diffusion distance (nm scale) along the grain boundary interfaces, before precipitation (cf. Ashby, 1972; Raj and Ashby, 1971). In metals GBS and GBM can be found to be coupled and sequential processes (Wilkinson and Cáceres, 1984). The fluid present along grain boundaries and pores can disperse as a result of local grain-scale pressure gradients resulting from the opening and closing of pores by GBS (Fusseis et al., 2009) (Fig. 9). Therefore, an interrelationship between the efficiency of GBS, GBM through dissolution-precipitation, local grain-scale stresses, and the availability of H_2O at grain boundaries can be expected. However, it is difficult to ascertain whether the pores were immediately filled by precipitating material or remained open for a certain duration of time, as we still do not fully understand the interdependence of these processes well enough. It is likely that the progressive weakening observed in novaculites or in Tana from dry to H_2O-added conditions (Fig. 8) can be correlated with a progressive increase in the effect of GBS throughout the samples. The efficiency of GBS should also be increased with decreasing grain size (Langdon, 2006) as more grain boundary surface becomes available for dissolution-precipitation. The strength difference

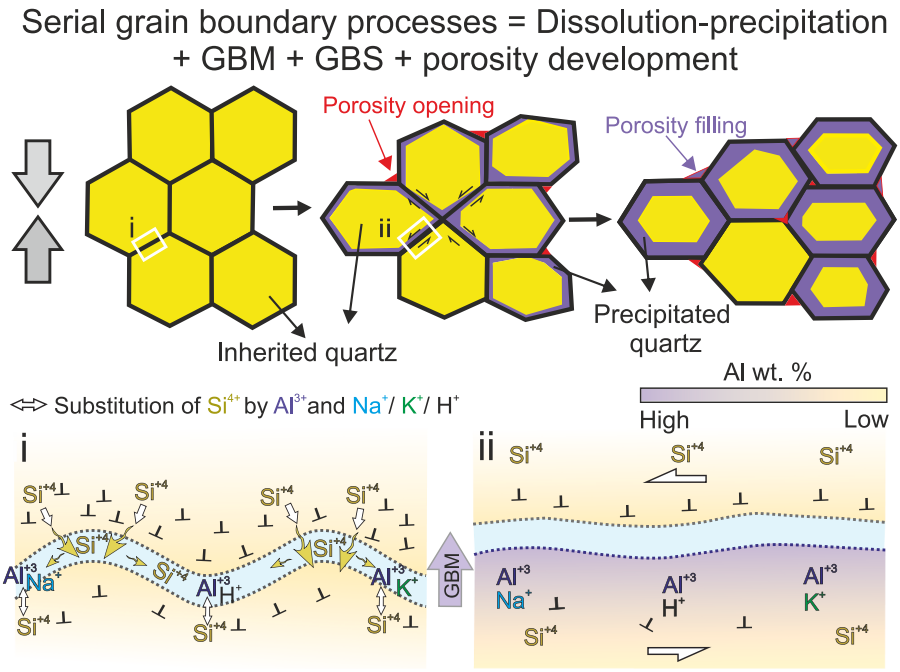

Fig. 9. Model of grain boundary processes occurring during plastic deformation of quartz aggregates. The undeformed grain boundaries were non-planner and the neighboring grains might have different dislocation densities (i). Dissolution-precipitation through grain boundary H_2O between adjacent grains and concurrent exchange of elements resulted in grain boundary migration (GBM) and the observed CL luminescence (ii). In a transient state, four-grain junctions and porosity can develop during grain boundary sliding (GBS). While the red colour indicates where porosity develops, the violet colour indicates the filling up of porosity with progressive deformation and precipitation.

between Tana and novaculite samples can be explained in this way (Fig. 7). If we consider the CL-blue colours and pervasive porosity development in the H_2O-added sample (Fig. 4a, b) as a proxy to the GBS mechanism facilitated by the dissolution-precipitation and GBM, then it is visibly clear that the CL-yellow patches in the as-is sample (Fig. 4d, e) and the top part of all the deformed samples (Fig. 7a) experienced less GBM and porosity development (Fig. 4a, Supplementary Fig. 7). It is probable that the initial water distribution controls the areas of grain coarsening in the as-is sample, and explains why the H_2O-added sample reach a more homogeneous GSD.

In the H_2O-added sample, the remaining yellow cores were of different sizes, asymmetric, and, in many cases, the whole grain may have been reconstituted (Fig. 4b). This observation implies that the present position of the boundaries between the yellow and dark/blue rims is not necessarily identical to the original grain boundary of the undeformed novaculite and suggests that the grain boundaries can also migrate inward and reconstitute at least parts of the grain interior. Multiple migration or sweeping of boundaries might be needed to substantially change the element concentration (Hay and Evans, 1987a; Negrini et al., 2014; Pearce and Wheeler, 2010) from the grain boundary to the interior (Fig. 7a). Hay and Evans (1987a, 1987b) described boundaries that migrated back and forth in response to the difference in chemical potential (the exact mechanism is unknown) and change the composition of calcite grains repeatedly by a process called chemically-induced grain boundary migration (CIGBM). Conversely, grain boundaries can sweep and reconstitute whole grains (Fig. 6a, e), as in strain-induced grain boundary migration (SIGBM) (Guillope and Poirier, 1979; Poirier and Guillopé, 1979). The potential energy that drives the SIGBM arises from the local difference in dislocation density. It is conceivable that the original grains (CL-yellow) have had a higher dislocation density than the reconstituted blue material and GBM (Fig. 6e) act as a recovery mechanism during deformation (Fig. 9). It has been argued that the internal distortion, thus, the dislocation density is greater in ice grains poorly oriented for easy slip. Such grains are consumed by neighbouring grains (suitably oriented for easy slip) with lower the dislocation density via GBM (Qi et al., 2017). SIGBM in a strict sense takes place without a change in chemical composition. Although, the low-angle (inner, sub-grain) boundaries observed in EBSD maps can act as pathways for ions. Previously, a comparable core-shell structure was numerically modelled for a plagioclase aggregate assuming a surface energy-driven GBM mechanism under hydrostatic stress (Pearce and Wheeler, 2010). Likewise, a core-shell structure is documented from fine quartz powder experiencing hydrostatic grain growth (Fig. 7i in Fukuda et al., 2019) and natural quartzite experiencing static annealing (Piazolo et al., 2005). Even though driving potentials can be different (surface versus strain energy), it is reasonable to assume that similar GBM processes operate during both creep and static grain growth. The chemical change of Al^{3+} substitution in quartz is very small; therefore, it is possible that SIGBM may provide the main driving potential for GBM (silica to dissolve in the grain boundary fluid) (Fig. 9), but contributions from CIGBM and surface energy cannot be ruled out.

Surprisingly, the addition of 0.1 wt.% H_2O induces a similar order of weakening in both Tana or novaculite samples (Fig. 8), although the grain boundary surface density is ~55 times higher in novaculite compared to Tana (considering the equivalent cube). It seems that it is not the amount of H_2O that is present in the grain boundaries and enters the crystal is affecting the strength (Kronenberg et al., 2020), and the original natural samples contain sufficient grain-scale H_2O for plastic deformation. Instead, it appears critical how much grain boundary surface area in the whole sample becomes reconstituted with available H_2O, contributing to the H_2O weakening (dry versus as-is versus H_2O-added). This conclusion is supported by the fact that the SIMS analysis of grain-scale H_2O count of the deformed quartz aggregate (Fig. 6d) did not show any significant variations between the as-is and H_2O-added samples, although they show a difference in mechanical strength (Fig. 2d). However, in the H_2O-added experiment (Fig. 4b), as much as 90 % of the image area became reconstituted (i.e., CL-blue) in ~27 h. In comparison, the as-is and dry samples that were deformed for more than six days showed less than 50 % reconstitution (Fig. 4). Therefore, grain coarsening, reconstitution of SiO_2, dispersion of H_2O,

and the development of porosity are linked. In the absence of H_2O (Fig. 6d) along the grain boundaries, the interrelationship between the dissolution-precipitation (GBM) and GBS has not been possible in the super-dry sample (Fig. 8), where the grain interiors are also too dry to show any evidence of plastic deformation (Griggs and Blacic, 1965) (Fig. 8, Supplementary Fig. 7). The limit, in terms of H_2O content, between deformable quartz material and the undeformable one, is between ~500 and ~750 H/10^6Si (Fig. 6d) (i.e., the highest point analysis concentration in OR116, and the lowest value of the undeformed novaculite). At laboratory strain rates and temperatures, similar range of water content values were also earlier reported for the absence of brittle deformation and fully crystal plastic deformation (Poirier, 1985; Kronenberg, 1994; Stünitz et al., 2017).

4.4. A grain-size-insensitivity quartz flow law linked to the microphysics

The fact that both the n and Q values of fine-grained novaculite are very similar to those of coarse-grained Tana quartzite irrespective of the H_2O content suggests that the n and Q values are grain-size-independent and that the same combination of deformation processes is active in experiments above a grain size of (d_{2D}) ~4 μm (d_{3D}~ 6μm). From EBSD mapping, it is evident that plastic strain (internal misorientations accompanied by the development of low angle inner and sub-grain boundaries) in the novaculite is achieved by crystal-plastic processes (Figs. 3, 4; Supplementary Fig. 3 a-c). It has been demonstrated that the bulk strain in Tana quartzite was achieved by intracrystalline deformation (Nègre et al., 2021). However, strain incompatibilities arising from an insufficient number of independent slip systems, and plastic anisotropy among neighbouring grains do not allow for homogeneous deformation (Hutchinson, 1976), even if individual grains become weaker by the infiltration of H_2O (Griggs and Blacic, 1965). Both, GBM and GBS may act as processes to remove such incompatibilities as accommodation mechanisms irrespective of the grain size to prevent hardening during dislocation glide. As explained in the above section, the strength difference between the Tana and novaculite samples can be explained by how much grain boundary area is available to become reconstituted by GBM through dissolution-precipitation and for GBS. Similar grain boundary accommodation mechanisms have been invoked to explain plasticity over a large grain size range in wet ice (Goldsby, 2006), halite (Bourcier et al., 2013), and in olivine (Hansen et al., 2011; Samae et al., 2021). As illustrated in earlier studies, GBM can also act as a recovery mechanism in addition to sub-grain formation during dynamic recrystallization in highly strained samples (Nègre et al., 2021). Diffusion of H_2O in quartz is very slow at an experimental time-scale (Kronenberg et al., 1986; Gerretsen et al., 1989) and H_2O transfer by microcracking in grains and grain boundary regions has been invoked for H_2O infiltration (FitzGerald et al. 1991; Stünitz et al., 2017). Our SIMS analyses indicate that GBM through dissolution-precipitation is another potential mechanism that allows H_2O to enter the quartz crystal. Moreover, it is known that the dissolution-precipitation process is pressure dependent (Manning, 1994, 2018) so that polycrystalline quartz becomes weaker with increasing confining pressure (Kronenberg and Tullis 1984; Holyoke and Kronenberg, 2010; Nègre et al., 2021; Stünitz et al., 2024).

Although grain size has an effect on the material strength (Tana versus novaculite), as the slope of the creep data (log-log and Arrhenius space) did not change for a considerable grain size range, it appears more practical to use different A-values to express the differences in strength as a proxy to the efficiency of the GBS mechanism. For example, the A-value for the 'as-is' coarse grained Tana sample ($d_{2D(mean)}$ = ~200 μm) will be ~4 times lower than the A-value reported for the H_2O-added Tana quartzite (= 1.56 × 10^{-6}/MPa/s) in Eq. (2). The A-value for a material similar to the as-is novaculite sample is the same as the A-value (= 1.56 × 10^{-6}/MPa/s) reported for the H_2O-added Tana. The A-value for a material similar to the H_2O-added novaculite sample ($d_{2D(mean)}$ = ~4 μm) is 4 times higher than the A-value for the H_2O-added Tana. Then, by simple linear approximation, the A-value for a H_2O-added quartz aggregate with a grain size of ~98 μm will be two times higher than the reported value in the Eq. (2). Alternatively, one may use the grain size exponent of 0.51 ± 0.13 from Fukuda et al. (2018).

4.5. How can the continental crust be weakened in order to facilitate shear localization?

Considering all differences in H_2O content and grain size, a maximum strength difference of about one order of magnitude is observed between the as-is Tana and H_2O-added novaculite (Fig. 8e). It suggests that a typical quartz-bearing crustal rock can be significantly softened by GSR (e.g., dynamic recrystallization) if there is an adequate amount of H_2O present to saturate the grain boundaries in the recrystallized fraction. Earlier the direct relationship between recrystallization processes and H_2O weakening in quartz has been inferred (Tullis and Yund, 1989). Therefore, the liberation of H_2O from the hydrous phases and from primary crystals by recrystallization (Fukuda et al., 2023) to the grain boundaries can be an effective strain localization method in nature and may start positive feedback in the shear zone (Finch et al., 2016). However, without a H_2O source or H_2O loss (Kronenberg et al., 2020) during deformation from the shear zone, only a modest weakening (~5 times) is expected (Fig. 7).

The original mechanical data (σ and $\dot{\varepsilon}$) reported in earlier constant-$\dot{\varepsilon}$ experiments (Fig. 8e) are measured from the peak stress or the steady state (after reaching peak stress) portion of the stress-strain curve. This means that the peak strength of the quartz aggregates (fine or coarse) can be reasonably predicted by our flow law (shaded region in Fig. 8e). However, a number of experiments show weakening in the stress-strain curve after the peak stress, for example, the typical regime 1 stress-strain curves (700 °C, 1.5 GPa and $\dot{\varepsilon} = 10^{-6}$ s^{-1}) from coarse-grained quartzite (Hirth and Tullis, 1992). The progressive weakening has been inferred to be a consequence of increasing amounts of dynamic recrystallization (bulges) along grain boundaries (Hirth and Tullis, 1992). As novaculite in this study has been chosen to represent a fully recrystallized (and recovered) material compared to a coarse-grained starting material, the maximum weakening at 100 % recrystallization in the quartzite should be limited by the novaculite mechanical data, as observed in Fig. 8e. However, it appears that even with 20–30 % of recrystallization (> 45–55 % strain), the quartzite stress-strain curve comes very close to that of the 0.17 wt.% H_2O-added novaculite curve (Fig. 3a of Hirth and Tullis, 1992). In shear experiments (800 °C, 1 Gpa and $\dot{\varepsilon} = \sim 2.5 \times 10^{-4}$ s^{-1}), Richter et al. (2018) observed that bulging recrystallization (regime 1) concentrates along shear bands. It is rational to assume that after significant shortening, geometrical softening by the development of foliations, SPO, CPO, shear bands, micro shear zones, etc. in the co-axial experiments are likely (Nègre et al., 2021; Pongrac et al., 2022). Therefore, the weakening observed in regime 1 of Hirth and Tullis (1992) and in other experiments after reaching the peak stress have a significant contribution from geometrical softening in addition to the GSR. These results indicate that 20 to 30 % of recrystallized material are sufficient to determine the mechanical behaviour by geometric weakening (Handy, 1994). As mentioned above, without a H_2O source the maximum weakening expected is ~5 times (Fig. 8e) the strength of the protolith by GSR. Therefore, if it can be demonstrated that a higher order of weakening (> half an order of magnitude) is needed for sustainable shear zone development, then factors like geometric softening are necessary. On the other hand, if GSR as observed from natural mylonitic rocks is the most important mechanism of strain localization, then only a modest weakening (~5 times) is required to develop sustainable plate boundary shear zones in the quartz-rheology dominated crust.

5. Conclusions

Our constant-load experiments demonstrate that the flow law parameters (stress exponent of $n \approx 2$ and activation energy of $Q = 110$ kJ/mol) of polycrystalline quartz are independent of the grain size variations (at the range of ~200 to ~3 μm). Grain size differences of this order of magnitude are generally observed in natural rocks. Our direct observational evidence from deformed fine-grained novaculites shows that the *n*-value of 2 represents a combination of serial processes involving grain boundary migration and grain boundary sliding as accommodation processes to obliterate strain incompatibilities resulting from dislocation glide in grain interiors. Furthermore, grain boundary migration by dissolution-precipitation can locally eliminate the strain incompatibilities at the grain boundaries and shape the grains in a way that is more suitable for grain boundary sliding. In these ways, the gain boundary processes may prevent strain hardening. The differences in the *A*-value between coarse- and fine-grained quartz (Tana and novaculites samples, respectively) can account for the differences in strength and grain size. The grain boundary processes in the presence of H_2O are the main accommodating mechanism in dislocation creep of quartz aggregates. These processes leave a chemical signature in the microstructure that can be resolved using techniques like cathodoluminescence and chemical mapping. Furthermore, drying to the extent of the super-dry sample suppress any sort of intra-grain plasticity, thus, the minimum amount of H_2O (472 to 766 H/10^6Si) needed for intra-grain plasticity can be constrained.

A comparison with the mechanical properties of deformed coarse-grained Tana quartzite from our earlier studies indicate that there will be no switch in deformation mechanisms by the grain size reduction. Consequently, we can expect a modest weakening of ~5 times the strength of the protolith if the grain size is reduced by dynamic recrystallization by two orders of magnitude. If a wet shear zone material from a protolith is produced involving geometric softening (development of foliations, SPO, CPO, shear bands, etc.), a significant weakening can be achieved. However, considering grain size reduction as the most effective mechanism of strain localization, our results suggest that maybe a lower amount of weakening is actually needed to make plate boundaries in the crust similar to the Earth than previously thought.

CRediT authorship contribution statement

Subhajit Ghosh: Writing – review & editing, Writing – original draft, Resources, Methodology, Investigation, Funding acquisition, Formal analysis, Data curation, Conceptualization, Validation, Visualization. **Holger Stünitz:** Writing – review & editing, Methodology, Investigation, Conceptualization. **Hugues Raimbourg:** Writing – review & editing, Investigation, Formal analysis, Data curation, Conceptualization. **Jacques Précigout:** Writing – review & editing, Methodology, Investigation, Data curation. **Ida Di Carlo:** Writing – review & editing, Investigation, Data curation. **Renée Heilbronner:** Methodology, Investigation, Formal analysis. **Laurette Piani:** Writing – review & editing, Investigation, Data curation.

Declaration of competing interest

The authors declare that they have no known competing financial interests or personal relationships that could have appeared to influence the work reported in this paper.

Data availability

All the data are submitted with the manuscript.

Acknowledgements

The novaculite samples from Arkansas was supplied by Corbin Cannon of Arkansas Geological Survey. The f_{H_2O} can be calculated from Tony Wither's fugacity calculator (https://publish.uwo.ca/~awither5/fugacity/index.htm), assuming the water pressure approximates the confining pressure during the deformation. We thank Sylvain Janiec (ISTO) for making and partly polishing thin sections. SG thanks Estelle Rose-Koga for her guidance during the preparation of samples for SIMS analysis. SG, HR and LP are grateful to the LG-SIMS-Nancy team for their technical help for SIMS measurements. We acknowledge the support from both LabEx VOLTAIRE (ANR-10-LABX-100-01) and EquipEx PLANEX (ANR-11-EQPX-0036) projects. This project has benefited from the expertise and the facilities of the Platform MACLE - CVL which was co-funded by the European Union and Centre-Val de Loire Region (FEDER). We thank A. Dimanov and an anonymous reviewer for their very constructive and insightful reviews that have substantially improved this manuscript. We are also thankful to J. P. Avouac for handling this manuscript.

Supplementary materials

Supplementary material associated with this article can be found, in the online version, at doi:10.1016/j.epsl.2024.118767.

References

Ashby, M.F., 1972. Boundary defects, and atomistic aspects of boundary sliding and diffusional creep. Surf. Sci. 31, 498–542.
Bercovici, D., Ricard, Y., 2016. Grain-damage hysteresis and plate tectonic states. Phys. Earth Planetary Interiors 253, 31–47. https://doi.org/10.1016/j.pepi.2016.01.005.
Bestmann, M., Pennacchioni, G., 2015. Ti distribution in quartz across a heterogeneous shear zone within a granodiorite: the effect of deformation mechanism and strain on Ti resetting. Lithos. 227, 37–56. https://doi.org/10.1016/j.lithos.2015.03.009.
Bishop, R.R., 1996. Grain Boundary Migration in Experimentally Deformed Quartz aggregates: The relationship Between Dynamically Recrystallized Grain Size and Steady State Flow Stress. Brown University, Providence, RI, p. 36.
Blacic, J.D., Christie, J.M., 1984. Plasticity and hydrolytic weakening of quartz single crystals. J. Geophys. Res. Solid. Earth. 89, 4223–4239.
Bourcier, M., Bornert, M., Dimanov, A., Héripré, E., Raphanel, J.L., 2013. Multiscale experimental investigation of crystal plasticity and grain boundary sliding in synthetic halite using digital image correlation. J. Geophys. Res. Solid Earth 118 (2), 511–526.
Coble, R.L., 1963. A model for boundary diffusion controlled creep in polycrystalline materials. J. Appl. Phys. 34, 1679–1682.
Dimanov, A., Rybacki, E., Wirth, R., Dresen, G., 2007. Creep and strain-dependent microstructures of synthetic anorthite-diopside aggregates. J. Struct. Geol. 29, 1049–1069. https://doi.org/10.1016/j.jsg.2007.02.010.
Finch, M.A., Weinberg, R.F., Hunter, N.J.R., 2016. Water loss and the origin of thick ultramylonites. Geology. 44, 599–602. https://doi.org/10.1130/G37972.1.
Fitz Gerald, J.D., Boland, J.N., McLaren, A.C., Ord, A., Hobbs, B.E., 1991. Microstructures in water-weakened single crystals of quartz. J. Geophys. Res. 96, 2139–2155. https://doi.org/10.1029/90JB02190.
Fukuda, J., Holyoke, C.W., Kronenberg, A.K., 2018. Deformation of fine-grained quartz aggregates by mixed diffusion and dislocation creep. J. Geophys. Res. Solid. Earth. 123, 4676–4696. https://doi.org/10.1029/2017JB015133.
Fukuda, J., Okudaira, T., Ohtomo, Y., 2023. Water release and homogenization by dynamic recrystallization of quartz. Solid Earth 14, 409–424. https://doi.org/10.5194/se-14-409-2023.
Fukuda, J., Raimbourg, H., Shimizu, I., Neufeld, K., Stünitz, H., 2019. Experimental grain growth of quartz aggregates under wet conditions and its application to deformation in nature. Solid Earth 10, 621–636. https://doi.org/10.5194/se-10-621-2019.
Fusseis, F., Regenauer-Lieb, K., Liu, J., Hough, R.M., De Carlo, F., 2009. Creep cavitation can establish a dynamic granular fluid pump in ductile shear zones. Nature 459, 974–977. https://doi.org/10.1038/nature08051.
Ghosh, S., Koizumi, S., Hiraga, T., 2021. Diffusion creep of diopside. J. Geophys. Res. Solid. Earth. 126 https://doi.org/10.1029/2020JB019855.
Ghosh, S., Stünitz, H., Raimbourg, H., Précigout, J., 2022. Quartz rheology constrained from constant-load experiments: consequences for the strength of the continental crust. Earth. Planet. Sci. Lett. 117814 https://doi.org/10.1016/j.epsl.2022.117814.
Gleason, G.C., Tullis, J., 1995. A flow law for dislocation creep of quartz aggregates determined with the molten salt cell. Tectonophysics. 247, 1–23. https://doi.org/10.1016/0040-1951(95)00011-B.
Goldsby, D.L., 2006. Superplastic flow of ice relevant to glacier and ice-sheet mechanics. Glacier Sci. Environ. Change 308–314.
Goldsby, D.L., Kohlstedt, D.L., 2001. Superplastic deformation of ice: experimental observations. J. Geophys. Res. Solid. Earth. 106, 11017–11030. https://doi.org/10.1029/2000jb900336.

Griggs, D., 1967. Hydrolytic weakening of quartz and other silicates. Geophys. J. Int. 14 (1–4), 19–31.
Griggs, D., 1974. A model of hydrolytic weakening in quartz. J. Geophys. Res. 79, 1653–1661.
Griggs, D.T., Blacic, J.D., 1965. Quartz: anomalous weakness of synthetic crystals. Science (1979) 147 (1979), 292–295.
Guillope, M., Poirier, J.P., 1979. Dynamic recrystallization during creep of single-crystalline halite: an experimental study. J. Geophys. Res. 84, 5557–5567. https://doi.org/10.1029/JB084iB10p05557.
Handy, M.R., 1994. The energetics of steady state heterogeneous shear in mylonitic rock. Mater. Sci. Eng. 175, 261–272. https://doi.org/10.1016/0921-5093(94)91065-0.
Hansen, L.N., Zimmerman, M.E., Kohlstedt, D.L., 2011. Grain boundary sliding in San Carlos olivine: flow law parameters and crystallographic-preferred orientation. J. Geophys. Res. Solid. Earth. 116 https://doi.org/10.1029/2011JB008220.
Hay, R.S., Evans, B., 1987a. Chemically induced grain boundary migration in calcite: temperature dependence, phenomenology, and possible applications to geologic systems. Contrib. Mineral. Petrol. 97, 127–141. https://doi.org/10.1007/BF00375220.
Hay, R.S., Evans, B., 1987b. Chemically induced migration in low and high angle calcite grain boundaries. Acta Metal. 35, 2049–2062.
Heilbronner, R., Kilian, R., 2017. The grain size(s) of Black Hills Quartzite deformed in the dislocation creep regime. Solid Earth 8, 1071–1093. https://doi.org/10.5194/se-8-1071-2017.
Herring, C., 1950. Diffusional viscosity of a polycrystalline solid. J. Appl. Phys. 21, 437–445.
Hier-Majumder, S., Mei, S., Kohlstedt, D.L., 2005. Water weakening of clinopyroxenite in diffusion creep. J. Geophys. Res. Solid. Earth. 110, 1–12. https://doi.org/10.1029/2004JB003414.
Hirth, G., Kohlstedt, D., 2004. Rheology of the upper mantle and the mantle wedge: a view from the experimentalists, in: geophysical Monograph Series. Blackwell Publ. Ltd 83–105. https://doi.org/10.1029/138GM06.
Hirth, G., Teyssier, C., Dunlap, W.J., 2001. An evaluation of quartzite flow laws based on comparisons between experimentally and naturally deformed rocks. Int. J. Earth Sci. 90, 77–87. https://doi.org/10.1007/s005310000152.
Hirth, G., Tullis, J., 1992. Dislocation creep regimes in quartz aggregates. J. Struct. Geol. 14, 145–159. https://doi.org/10.1016/0191-8141(92)90053-Y.
Holyoke III, C.W., Kronenberg, A.K., 2010. Accurate differential stress measurement using the molten salt cell and solid salt assemblies in the Griggs apparatus with applications to strength, piezometers and rheology. Tectonophysics. 494 (1–2), 17–31. https://doi.org/10.1016/j.tecto.2010.08.001.
Holyoke III, C.W., Kronenberg, A.K., 2013. Reversible water weakening of quartz. Earth Planet. Sci. Lett. 374, 185–190.
Hutchinson, J.W., 1976. Bounds and self-consistent estimates for creep of polycrystalline materials. Proc. R. Soc. Lond. A 348, 101–127.
Jaoul, O., Tullis, J., Kronenberg, A., 1984. Effect of varying water contents on the creep behavior of Heavitree quartzite. J. Geophys. Res. 4298–4312. https://doi.org/10.1029/jb089ib06p04298.
Karato, S., 2008. Deformation of Earth Materials. Cambridge University Press. https://doi.org/10.1017/CBO9780511804892.
Kidder, S., Hirth, G., Avouac, J.P., Behr, W., 2016. The influence of stress history on the grain size and microstructure of experimentally deformed quartzite. J. Struct. Geol. 83, 194–206. https://doi.org/10.1016/j.jsg.2015.12.004.
Koch, P.S., Christie, J.M., Ord, A., George, R.P., 1989. Effect of water on the rheology of experimentally deformed quartzite. J. Geophys. Res. 94 https://doi.org/10.1029/jb094ib10p13975.
Kronenberg, A.K., Ashley, K.T., Francsis, M.K., Holyoke III, C.W., Jezek, L., Kronenberg, J.A., Law, R.D., Thomas, J.B., 2020. Water loss during dynamic recrystallization of Moine thrust quartzites, northwest Scotland. Geology. 48, 557–561. https://doi.org/10.1130/G47041.1.
Kronenberg, A.K., 1994. Hydrogen speciation and chemical weakening of quartz. Rev. Mineral. Geochem. 29 (1), 123–176.
Kronenberg, A.K., Tullis, J., 1984. Flow strengths of quartz aggregates: grain size and pressure effects due to hydrolytic weakening. J. Geophys. Res. 4281–4297. https://doi.org/10.1029/jb089ib06p04281.
Langdon, T.G., 2006. Grain boundary sliding revisited: Developments in sliding over four decades. J. Mater. Sci. 41, 597–609.
Luan, F.C., Paterson, M.S., 1992. Preparation and deformation of synthetic aggregates of quartz. J. Geophys. Res. 97, 301–320. https://doi.org/10.1029/91JB01748.
Menegon, L., Fusseis, F., Stünitz, H., Xiao, X., 2015. Creep cavitation bands control porosity and fluid flow in lower crustal shear zones. Geology. 43, 227–230. https://doi.org/10.1130/G36307.1.
Nabbarro, F.R.N., 1948. Deformation of crystals by motion of single ions. In: Report on a Conference on the Strength of Solids. The Physical Society.
Nègre, L., Stünitz, H., Raimbourg, H., Lee, A., Précigout, J., Pongrac, P., Jeřábek, P., 2021. Effect of pressure on the deformation of quartz aggregates in the presence of H2O. J. Struct. Geol. 148 https://doi.org/10.1016/j.jsg.2021.104351.
Negrini, M., Stunitz, H., Berger, A., Morales, L.F.G., 2014. The effect of deformation on the TitaniQ geothermobarometer: an experimental study. Contrib. Mineral. Petrol. 167, 1–22. https://doi.org/10.1007/s00410-014-0982-x.
Paterson, M.S., 2012. Materials Science For Structural Geology. Springer Science & Business Media.
Paterson, M.S., Luan, F.C., 1990. Quartzite rheology under geological conditions. Geol. Soc., Lond., Spec. Publ. 54, 299–307.
Pearce, M.A., Wheeler, J., 2010. Modelling grain-recycling zoning during metamorphism. J. Metamorph. Geol. 28, 423–437. https://doi.org/10.1111/j.1525-1314.2010.00872.x.
Perny, B., Eberhardt, P., Ramseyer, K., Mullis, J., Pankrath, R., 1992. Microdistribution of Al, Li, and Na in α quartz: possible causes and correlation with short-lived cathodoluminescence. Am. Mineral. 77, 534–544.
Piazolo, S., Prior, D.J., Holness, M.D., 2005. The use of combined cathodoluminescence and EBSD analysis: a case study investigating grain boundary migration mechanisms in quartz. J. Microsc. 217, 152–161.
Poirier, J.-P., Guillopé, M., 1979. Deformation induced recrystallization of minerals. Bulletin de Mineralogie 102, 67–74.
Poirier, J.P., 1985. Creep of Crystals: High-Temperature Deformation Processes in Metals, Ceramics and Minerals. Cambridge Univ. Press, Cambridge, U. K, p. 260.
Pongrac, P., Jeřábek, P., Stünitz, H., Raimbourg, H., Heilbronner, R., Racek, M., Nègre, L., 2022. Mechanical properties and recrystallization of quartz in presence of H2O: combination of cracking, subgrain rotation and dissolution-precipitation processes. J. Struct. Geol. 160 https://doi.org/10.1016/j.jsg.2022.104630.
Précigout, J., Stünitz, H., Pinquier, Y., Champallier, R., Schubnel, A., 2018. High-pressure, high-temperature deformation experiment using the new generation griggs-type apparatus. J. Vis. Exp. 2018 https://doi.org/10.3791/56841.
Qi, C., Goldsby, D.L., Prior, D.J., 2017. The down-stress transition from cluster to cone fabrics in experimentally deformed ice. Earth. Planet. Sci. Lett. 471, 136–147. https://doi.org/10.1016/j.epsl.2017.05.008.
Raimbourg, H., Rajič, K., Moris-Muttoni, B., Famin, V., Palazzin, G., Fisher, D., Morell, K., Erdmann, S., Di Carlo, I., Montmartin, C., 2021. Quartz vein geochemistry records deformation processes in convergent zones. Geochem., Geophys., Geosyst. 22 https://doi.org/10.1029/2020GC009201.
Raj, R., Ashby, M.F., 1971. On grain boundary sliding and diffusional creep. Metal. Trans. 2, 1113–1127.
Richter, B., Stünitz, H., Heilbronner, R., 2018. The brittle-to-viscous transition in polycrystalline quartz: an experimental study. J. Struct. Geol. 114, 1–21. https://doi.org/10.1016/j.jsg.2018.06.005.
Rutter, E.H., Brodie, K.H., 2004a. Experimental grain size-sensitive flow of hot-pressed Brazilian quartz aggregates. J. Struct. Geol. 26 https://doi.org/10.1016/j.jsg.2004.04.006, 2011–2023.
Rutter, E.H., Brodie, K.H., 2004b. Experimental intracrystalline plastic flow in hot-pressed synthetic quartzite prepared from Brazilian quartz crystals. J. Struct. Geol. 26, 259–270. https://doi.org/10.1016/S0191-8141(03)00096-8.
Rutter, E.H., Brodie, K.H., 1988. The role of tectonic grain size reduction in the rheological stratification of the lithosphere. Geologische Rundschau 77, 295–307. https://doi.org/10.1007/BF01848691.
Rybacki, E., Paterson, M.S., Wirth, R., Dresen, G., 2003. Rheology of calcite–quartz aggregates deformed to large strain in torsion. J. Geophys. Res. Solid. Earth. 108 https://doi.org/10.1029/2002jb001833.
Samae, V., Cordier, P., Demouchy, S., Bollinger, C., Gasc, J., Koizumi, S., Mussi, A., Schryvers, D., Idrissi, H., 2021. Stress-induced amorphization triggers deformation in the lithospheric mantle. Nature 591, 82–86. https://doi.org/10.1038/s41586-021-03238-3.
Schmid, S.M., 1982. Laboratory experiments on rheology and deformation mechanisms in calcite and their application to studies in the field. Mitteilungen des Geologischen Institutes der ETH Universität. Zürich 241, 1.
Stipp, M., Fügenschuh, B., Gromet, L.P., Stünitz, H., Schmid, S.M., 2004. Contemporaneous plutonism and strike-slip faulting: a case study from the Tonale fault zone north of the Adamello pluton (Italian Alps). Tectonics. 23 https://doi.org/10.1029/2003TC001515.
Stipp, M., Tullis, J., Behrens, H., 2006. Effect of water on the dislocation creep microstructure and flow stress of quartz and implications for the recrystallized grain size piezometer. J. Geophys. Res. Solid. Earth. 111 https://doi.org/10.1029/2005JB003852.
Stünitz, H., Raimbourg, H., Nègre, L., Précigout, J., Jollands, M., Pongrac, P., Jeřabek, P., Gies, N., Lüder, M., 2024. Evolution of H_2O content in deforming quartz aggregates: An experimental study. J. Struct. Geol. 178, 105029.
Stünitz, H., Thust, A., Heilbronner, R., Behrens, H., Kilian, R., Tarantola, A., Fitz Gerald, J.D., 2017. Water redistribution in experimentally deformed natural milky quartz single crystals—implications for H2O-weakening processes. J. Geophys. Res. Solid. Earth. 122, 866–894. https://doi.org/10.1002/2016JB013533.
Tailby, N.D., Cherniak, D.J., Watson, E.B., 2018. Al diffusion in quartz. Am. Mineral. 103, 839–847. https://doi.org/10.2138/am-2018-5613.
Tokle, L., Hirth, G., Behr, W.M., 2019. Flow laws and fabric transitions in wet quartzite. Earth. Planet. Sci. Lett. 505, 152–161. https://doi.org/10.1016/j.epsl.2018.10.017.
Tullis, J., Yund, R.A., 1989. Hydrolytic weakening of quartz aggregates: the effects of water and pressure on recovery. Geophys. Res. Lett. 16 (11), 1343–1346.
Tullis, J., Yund, R.A., 1982. Grain growth kinetics of quartz and calcite aggregates. J. Geol. 90 (3), 301–318.
Urai, J.L., Means, W.D., Lister, G.S., 1986. Dynamic recrystallization of minerals. Mineral Rock Deform. 36, 161–199.
White, S.H., Burrows, S.E., Carreras, J., Shaw, N.D., Humphreys, F.J., 1980. On mylonites in ductile shear zones. J. Struct. Geol. 2, 175–187. https://doi.org/10.1016/0191-8141(80)90048-6.
Wilkinson, D.S., Cáceres, C.H., 1984. On the mechanism of strain-enhanced grain growth during superplastic deformation. Acta Metallurgica 32, 1335–1345. https://doi.org/10.1016/0001-6160(84)90079-8.
Yabe, K., Sueyoshi, K., Hiraga, T., 2020. Grain-boundary diffusion creep of olivine: 1. Experiments at 1 atm. J. Geophys. Res. Solid. Earth. 125 https://doi.org/10.1029/2020JB019415.
Yuan, M.-W., Li, L., Alam, M., Santosh, M., Li, S.-R., Hou, Z.-Q., 2023. Correlations between cathodoluminescence intensity and aluminum concentration in low-temperature hydrothermal quartz. Am. Mineral. 108, 1224–1231. https://doi.org/10.2138/am-2022-8471.